THE ASTROPHYSICAL JOURNAL, 452:407–422, 1995 October 10

A SEMIEMPIRICAL DETERMINATION OF THE WIND VELOCITY STRUCTURE FOR THE HYBRID-CHROMOSPHERE STAR α TRIANGULI AUSTRALIS[1]

GRAHAM M. HARPER, BRIAN E. WOOD, JEFFREY L. LINSKY,[2] AND PHILIP D. BENNETT
Joint Institute for Laboratory Astrophysics, University of Colorado and National Institute of Standards and Technology, Boulder, CO 80309-0440;
gmh@capybara.colorado.edu, wood@marmot.colorado.edu, jlinsky@jila.colorado.edu, and pbennett@capybara.colorado.edu

AND

THOMAS R. AYRES AND ALEXANDER BROWN
Center for Astrophysics and Space Astronomy, Department of Astrophysical, Planetary and Atmospheric Sciences, University of Colorado, Boulder, CO 80309-0389;
ayres@vulcan.colorado.edu, ab@echidna.colorado.edu
Received 1994 November 3; accepted 1995 April 24

ABSTRACT

We have used the Goddard High-Resolution Spectrograph (GHRS) on the *Hubble Space Telescope* to study the wind of the hybrid-chromosphere star α TrA (K4 II). The stellar wind produces significant absorption at negative radial velocities in the chromospheric Mg II resonance lines (*h* and *k*). Spectra obtained with the GHRS echelle high-resolution grating ($\lambda/\Delta\lambda \approx 85{,}000$) on 1993 February 10 and 1994 May 1 reveal complex interstellar absorption in the Mg II emission lines and a high-velocity wind absorption feature centered near -95 km s^{-1}. The 1993 February observation shows an asymmetry of the Mg II emission cores, corresponding to an apparent redshift of 6.0 ± 1.5 km s^{-1}. We construct a simple wind model that explains several of the key observational features. The scattering of the Mg II *h* and *k* photons in a geometrically extended region dominates the observed flux near line center, which supports the assignment of the low-velocity absorption components to interstellar absorption rather than to a chromospheric self-reversal. For the 1993 February observation, the parameters for our simple wind model are as follows: terminal velocity $V(\infty) = 100$ km s^{-1}, turbulent velocity $V_{\rm turb} = 24$ km s^{-1}, $\dot{M} \sim 1.8 \times 10^{-10}\ M_\odot$ yr^{-1}, for a fixed value of the velocity-law parameter $\beta = 1$ and fixed stellar radius of $R_* = 97\ R_\odot$, assuming Mg II is the dominant ionization state in the flow. Our analysis of the 1994 May observation resulted in similar values for these parameters, and the mass-loss rate could be as small as $\dot{M} \sim 1.6 \times 10^{-10}\ M_\odot$ yr^{-1}. The value of β is uncertain (≥ 0.3) and if $\beta \sim 3.5$ as found from the recent analysis of the ζ Aurigae systems, $\dot{M}$ could be larger by a factor of 3–4. A comparison of our result with numerical solutions to the momentum and conservation equations reveals that the derived velocity distribution lies within a limited region of parameter space where there is a large nonthermal pressure on the plasma close to the base of the wind consistent with previous wind models for α TrA. Our best model fit to the two interstellar absorption components indicates a total hydrogen column density toward α TrA of $N_{\rm H\,I} = 2 \times 10^{19}$ cm^{-2}.

Subject headings: line: formation — stars: chromospheres — stars: individual (α Trianguli Australis) — stars: late-type — stars: mass loss — ultraviolet: stars

1. INTRODUCTION

Ultraviolet spectra of late-type giants obtained early in the *International Ultraviolet Explorer* (*IUE*) mission led Linsky & Haisch (1979) to propose that a "coronal dividing line" exists in the Hertzsprung-Russell (H-R) diagram near spectral type K2 III. As confirmed by X-ray observations (e.g., Ayres et al. 1981; Haisch, Schmitt, & Rosso 1991), the division separates the earlier spectral type giants, which show evidence for hot plasma (transition regions and coronae), from the later spectral types, which show little evidence for plasma hotter than about 10,000 K but instead have cool winds identified, for example, by blueshifted absorption features in the Mg II resonance lines. The apparent division in the H-R diagram lies close to the region where stars with double absorption features are observed in the Mg II and Ca II resonance lines (Reimers 1982). This part of the H-R diagram is also the location where the ratio of fluxes in the red (F_R) and blue (F_V) emission peaks of the Mg II and Ca II resonance lines changes from $F_R/F_V < 1$ on the left to $F_R/F_V > 1$ on the right (Stencel & Mullan 1980a, b), indicating a change in the stellar wind properties.

In apparent disagreement with this empirical picture, Hartmann, Dupree, & Raymond (1980) identified a class of stars, which they called "hybrid-chromosphere," that presents evidence for both 10^5 K plasma (e.g., the C IV doublet at 1549 Å) and cool ($T < 10^4$ K), moderate-velocity ($V \sim 100$ km s^{-1}) winds. The hybrids consist of G-type supergiants like α Aqr (G2 Ib) and K-type bright giants like α TrA (K4 II). These intermediate mass stars (3–10 $M_\odot$) probably have different internal structures and dynamos than the lower mass luminosity class III giants that provided the original evidence for a dividing line; the mass of α TrA, for example, has been estimated to be $9.7 \pm 5\ M_\odot$ (Harper 1992a). Hartmann, Dupree,

[1] This work is based on observations made with the NASA/ESA *Hubble Space Telescope*, obtained at the Space Telescope Science Institute, which is operated by the Asssociation of Universities for Research in Astronomy, Inc., under NASA contract NAS 5-26555.

[2] Staff Member, Quantum Physics Division, National Institute of Standards and Technology.

& Raymond (1981) proposed that a low-velocity absorption component (typically near -20 km s^{-1}) seen in the Mg II resonance lines of hybrid stars in a chromospheric blueshifted self-reversal. This assignment was based on the presence of similar low-velocity Mg II components in α Aqr, β Aqr, and λ Vel. Hartmann et al. (1981) applied the Alfvén-wind-driven stellar wind theory of Hartmann & McGregor (1980) to α TrA to model its stellar wind and the strengths and widths of the higher temperature Si III], C III], and C IV lines. They determined mass-loss rates of about 4–5 $\times$ 10^{-9} $M_\odot$ yr^{-1}. Several other studies based on this theory subsequently were applied to α TrA, by, e.g., Mendoza (1984) and Krogulec (1989).

Drake, Brown, & Linsky (1984) presented a strong case that the low-velocity absorption components seen in the Mg II profiles of the hybrid stars are in fact interstellar, rather than circumstellar, features. In particular, there is close agreement between the observed velocities and line-of-sight interstellar velocities predicted from either a global interstellar flow vector or from measured interstellar medium (ISM) absorption toward adjacent hot stars. Furthermore, the low-velocity features are narrow and do not change with time, unlike the high-velocity wind features that are broad and variable.

Hartmann et al. (1985) constructed hydrostatic models for the high-temperature gas in the atmospheres of hybrid stars using an emission measure analysis with electron densities determined primarily from the C II] multiplet at 2325 Å. They noted that all of the lines in the O I 1304 Å triplet, and not just the 1302 Å line from the ground state, show profile asymmetries suggestive of motions in the O I line scattering region. They also found variability of the high-velocity absorption component on 4–6 month timescales. Their model for α TrA was extended by Brown et al. (1991) to include a $\geq 10^6$ K corona when X-rays from the star were discovered by *EXOSAT*. Brosius & Mullan (1986) also constructed models of the transition regions of six hybrid bright giant and supergiants based on the analysis of *IUE* data. These models included the effects of mass-loss and were found to be consistent with the models of Hartmann et al. (1985). Based on the *ROSAT* all-sky survey data set, Haisch, Schmitt, & Rosso (1992) reported X-ray emission from α TrA and another hybrid star δ And. The presence of X-rays poses the question of how α TrA can have both hot plasma and a cool wind, unlike the Sun, which has a hot corona and a hot, high-speed coronal wind. Does the hot plasma lie at the turbulent base of the cool wind as proposed by Hartmann et al. (1985) and Brosius & Mullan (1986)? Or does the hot plasma exist only in magnetically confined regions that are physically separate from the cool wind (perhaps located in regions with open field lines) as proposed by Reimers (1982) and by Linsky (1982)? The discovery of an X-ray flare on α TrA (Kashyap 1993; Kashyap et al. 1994) would seem to suggest that the hybrid star possesses complex coronal magnetic structures like those of solar active regions. The uncertain interpretation of the low-velocity features and the observation that the optically thin intersystem lines of C II], C III], and Si III] show no significant Doppler shifts (Brown, Reimers, & Linsky 1986), indicating that hotter plasma might not participate in the outflow, have stimulated the observing program and analysis in the present paper.

In § 2 we discuss our *Hubble Space Telescope*/Goddard High-Resolution Spectrograph (*HST*/GHRS) observations of α TrA and analyze the far-UV emission lines of the 1880–1920 Å region, in § 3 we derive the parameters of the two ISM features, and in § 4 we discuss the semiempirical wind model based on the Mg II resonance line profiles. Section 4 also includes a brief study of the physical conditions which can lead to the deduced wind velocity distribution. In § 5 we compile and discuss the velocity information for the wind and atmosphere of α TrA, and we present the conclusions in § 6.

2. GODDARD HIGH-RESOLUTION SPECTROGRAPH OBSERVATIONS

The GHRS on the *HST*, with its high spectral resolution, high signal-to-noise ratio, and low scattered light, is ideal for the study of stellar wind features of hybrid-chromosphere stars. For a description of the GHRS, see Brandt et al. (1994) and Duncan (1992). We observed α Trianguli Australis (α TrA = HR 6217 = HD 150798) through the GHRS large science aperture (LSA) on 1993 February 10 (prior to the installation of the COSTAR corrective optics) and then obtained a post-COSTAR spectrum of the Mg II *h* and *k* line taken through the small science aperture (SSA) on 1994 May 1. These observations are summarized in Table 1.

The Mg II *h* and *k* lines obtained in 1993 February 10 are shown on a stellar rest frame velocity scale in Figure 1 (λ_{air} 2802.705 Å and 2795.528 Å; Morton 1991). The stellar radial velocity is taken to be -3.4 km s^{-1} (Mayor & Maurice 1985). The present paper deals mostly with the high-resolution observations of the Mg II lines. However, the two moderate-resolution spectra (1536–1572 Å and 1879–1920 Å) are also illustrated with line identifications in Figure 2. We could not positively identify the features seen in the 1535–1545 Å spectral region, but there are numerous Si I lines in this region identified in the solar spectrum (Moore et al. 1977), as well as possible fluoresced bands of the CO fourth-positive system.

2.1. *The* Mg II *h and k Line Profiles*

The LSA GHRS spectra were processed using the 1993 September version of the CALHRS calibration software (Duncan

TABLE 1

SUMMARY OF GODDARD HIGH-RESOLUTION SPECTROGRAPH OBSERVATIONS OF α TRIANGULI AUSTRALIS

Grating	Spectral Range (Å)	Spectral Res. (km s^{-1})	Exposure Time (s)	Start Time (UT)	Important Features
1993 *February 10 observations*:					
G160M.....	1536–1572	20	3554	03:37	C IV
G200M.....	1879–1920	20	2370	05:31	Si III], C III]
EB-20	2792–2807	3.5	431	06:48	Mg II
1994 *May 1 observation*:					
EB-20	2789–2804	3.5	326	18:23	Mg II

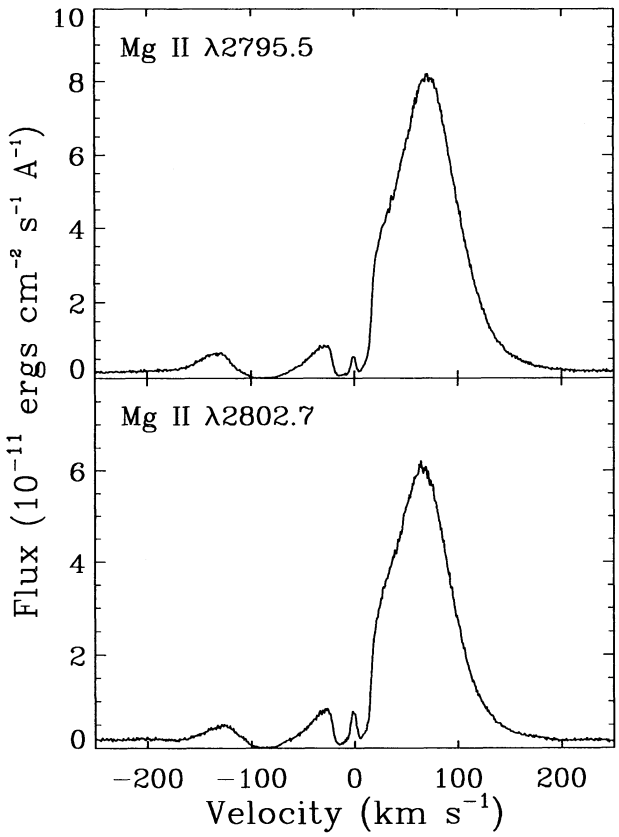

FIG. 1.—High-resolution echelle B spectra of the Mg II resonance lines of α TrA obtained 1993 February 10. The velocity scale is in the stellar rest frame. The wind absorption is centered near −95 km s^{-1}, and the two interstellar Mg II absorption components centered at heliocentric velocities of −17 and +3 km s^{-1} are also apparent.

1992). A wavelength calibration spectrum was obtained before each spectrum to obtain an accurate zero-point shift. For the calibration spectrum obtained prior to the Mg II spectrum, 10 Pt lamp lines were used to determine the calibration coefficients. The rms deviation of the observed line positions from the calculated fit is 0.055 diodes, which is only 2 mÅ or 0.2 km s^{-1}. The CALHRS routine's flux calibration comes from the GHRS Science Verification Program (Ebbets 1992). The measured fluxes for the Mg II lines, which should be accurate to ±5%–10%, are $F_k = 5.85 \times 10^{-11}$ ergs cm^{-2} s^{-1}, $F_k^{\rm corr} = 6.50 \times 10^{-11}$ ergs cm^{-2} s^{-1}; $F_h = 4.20 \times 10^{-11}$ ergs cm^{-2} s^{-1}, $F_h^{\rm corr} = 4.73 \times 10^{-11}$ ergs cm^{-2} s^{-1}, where the superscript "corr" refers to our estimate of the flux after correcting for the intersellar attenuation (see § 3).

Figure 3 presents the observed post-COSTAR SSA Mg II *k* line profile. The SSA observation was reduced from the Guest Observer (GO) tape file using specialized software (written by T. R. Ayres) independent of the GHRS team package. The contemporaneous wavelength calibration indicated a small zero-point shift (−2.0 ± 0.2 km s^{-1}) which was subtracted from the assigned wavelength scales. Because the observations was taken through the SSA, the absolute flux scale is uncertain. The integrated Mg II line fluxes in the SSA spectrum are a factor of 1.9 fainter than the LSA spectrum. The latter agrees with many *IUE* echelle spectra of α TrA, which also show that the temporal fluctuations in the integrated Mg II fluxes are typically less than 10% (1 σ; see, e.g., Ayres et al. 1995). We conclude that the star must have been slightly off center in the SSA. Indeed, SSA and LSA G160M spectra of the H I Lyα line of α TrA, taken shortly after the Mg II observation, also show a significant reduction in the SSA flux scale (≃0.7 LSA). These data will be discussed elsewhere. We therefore adjust the Mg II SSA flux scale upward (by a factor of 1.9) so that the "continuum" bands at 2792 ± 1 Å and 2800 ± 1 Å agree with the LSA observation, which should be insensitive to small pointing errors. Superposed on the observed SSA profile in Figure 3 are two curves which represent different levels of resolution degradation. The solid curve is a convolution of the observed SSA profile with the pre-COSTAR echelle-B LSA point-spread function (PSF) (Gilliland & Hulbert 1993) to simulate the resolution of our earlier LSA observation (Fig. 1). The dotted curve is the convolution of the observed profile with a Gaussian of full width at half-maximum (FWHM) = 25 km s^{-1}, representing the resolution of optimum *IUE* echelle observations. It can be seen that the two low-velocity absorption features, which we believe are interstellar, should not be resolved in *IUE* data in accord with observations.

We find that when we reflect the wings of the LSA line profiles (beyond ±140 km s^{-1} from line center) about the central wavelengths, the profiles appear shifted with respect to the photospheric velocity frame. The 6.0 ± 1.5 km s^{-1} shift of the emission peaks is in the same sense for both the Mg II *h* and *k* lines. Unfortunately, there are no other well-defined features in the limited bandpass echelle spectrum to provide further velocity information. We do not see the same shift in the SSA observation. The star α TrA is an IAU radial velocity standard, and although there appears to be some temporal variation (−3.4 ± 0.4 km s^{-1}; Mayor & Maurice 1985), it is much smaller than the shift we detect here. We believe that the apparent 6 km s^{-1} shift of the Mg II *h* and *k* emission peaks is probably real rather than an instrumental artifact. The expected 1 σ velocity errors for GHRS echelle SSA spectra obtained after an observation of the Pt wavelength calibration lamp are about 1.5 km s^{-1} (see discussion in Linsky et al. 1993). The Mg II observations, however, were obtained through the LSA which has dimensions of 2″ × 2″. Miscentering of the star in the LSA by 0″.43 would produce a velocity error of 6 km s^{-1}, but miscenterings that large are unusual. As described in the next section, we find an interstellar absorption feature centered at −17.3 km s^{-1} which we believe is due to the V^G cloud whose line-of-sight velocity toward α TrA is −16.7 km s^{-1}. The 0.6 km s^{-1} difference between the measured and expected interstellar absorption velocity is consistent with the expected precision of the data.

Since the thermalization lengths for the Mg II *h* and *k* lines are much smaller than the stellar radius (Harper 1992b), the observed velocity shifts may result from rising or falling plasmas that have quite different emissivities. Global shifts such as those that occur in pulsating stellar atmospheres are also a possibility. Indeed, Rao et al. (1993) have suggested that the hybrid-chromosphere bright giants might pulsate, albeit erratically, on the basis of the variability of the Ca II H and K lines. A separate high-velocity wind component that absorbs some of the emission in the far blue wings of the Mg II lines might also explain the apparent line redshifts. We note that Hartmann et al. (1985) have detected wind absorption out to −180 km s^{-1} in *IUE* spectra and that the observed timescales for variability in the wind profiles are consistent of multiple wind components within the scattering region at one time (see § 4.2.2).

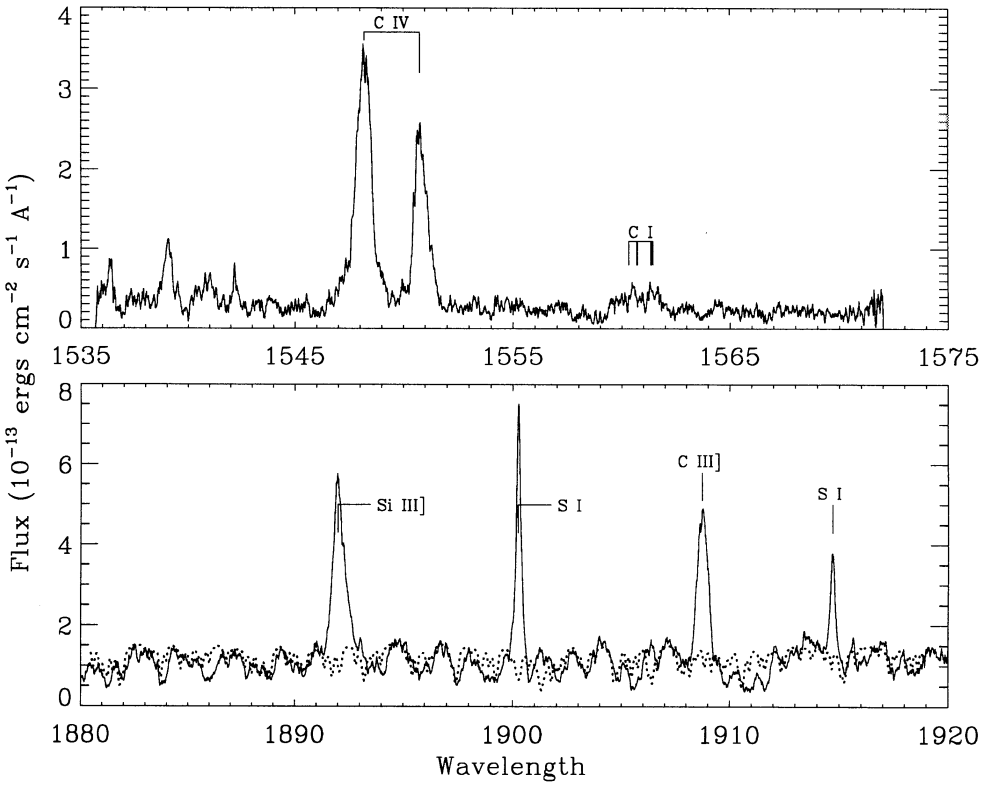

FIG. 2.—The two moderate-resolution spectra of α TrA with line identifications. The top frame is the G160 spectrum, and the lower frame is the G200M spectrum. Superposed on the G200M spectrum is the continuum model described in § 2.2.

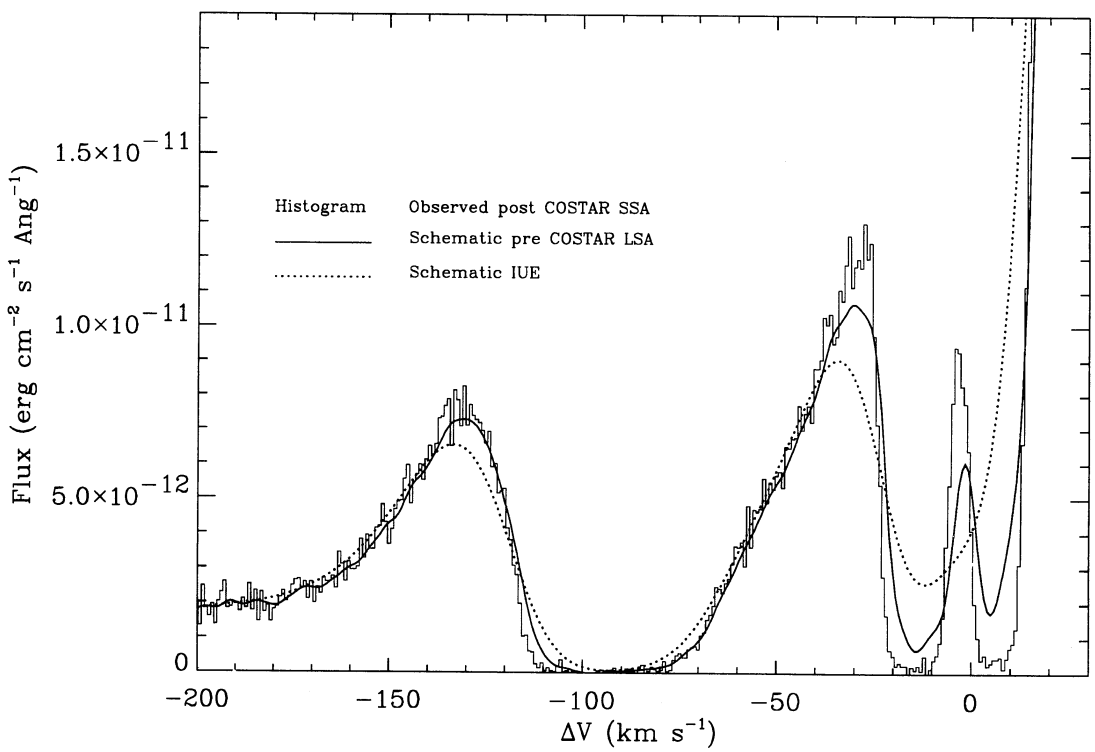

FIG. 3.—Comparison of a small science aperture (SSA) post-COSTAR Mg II *h* line profile (*histogram*) with the same profile degraded in resolution to mimic (1) a pre-COSTAR large science aperture (LSA) observation, and (2) an *IUE* high-resolution observation. The velocity scale is in the stellar rest frame.

Figure 4 shows a comparison of the post-COSTAR SSA observation for the Mg II *k* line with the pre-COSTAR observation. For comparison, the post-COSTAR observation has been degraded in resolution to match the pre-COSTAR LSA spectrum and is scaled in flux as described previously. The post-COSTAR SSA observation shows a narrower but brighter red emission feature. In the SSA spectrum the red wing of the Mg II *k* line appears blueshifted relative to the LSA spectrum, but the far blue emission edges of the two spectra are aligned and the outer edges of the SSA profile are symmetric in the photospheric reference frame. The sharp ISM features of both spectra are aligned, to within the combined uncertainties of the wavelength scales, which further suggests that the profile differences between the two spectra are real. The agreement between the wavelength scales also suggest that the miscentering in the SSA probably was normal to the dispersion direction. We do not know why the far blue emission features overlap even though the line width has apparently changed between the observations.

In the LSA spectrum, the wings of the Mg II lines are not symmetric about line center. This is not the case for the SSA spectrum. When the mean flow velocity of a turbulent atmosphere is much smaller than the characteristic turbulence, the wings of an optically thin emission line will be symmetric about line center; i.e., there will be equal amounts of emission from the upward and downward moving components. *HST* echelle observations of α Tau have shown that this may not be the case in the chromosphere of that evolved late-type star. The velocity centroids of the optically thin C II] lines show an apparent down-flow of 4 km s^{-1} compared to the Doppler width of the line ($\simeq$0.6 FWHM) of $\simeq$14 km s^{-1} (Carpenter et al. 1991). Judge (1994) has also found evidence for a distribution of electron density as a function of velocity. The portions of the α TrA LSA Mg II line profiles that show the reflection asymmetry respond to the source function in the lower chromosphere where it begins to follow the chromospheric temperature rise. Observations of the optically thin lines of the C II] 2325 Å multiplet would significantly improve our understanding of the velocity structure: these lines form at depths that overlap the region where the Mg II photons at the edge of the emission core are last scattered before escaping the atmosphere.

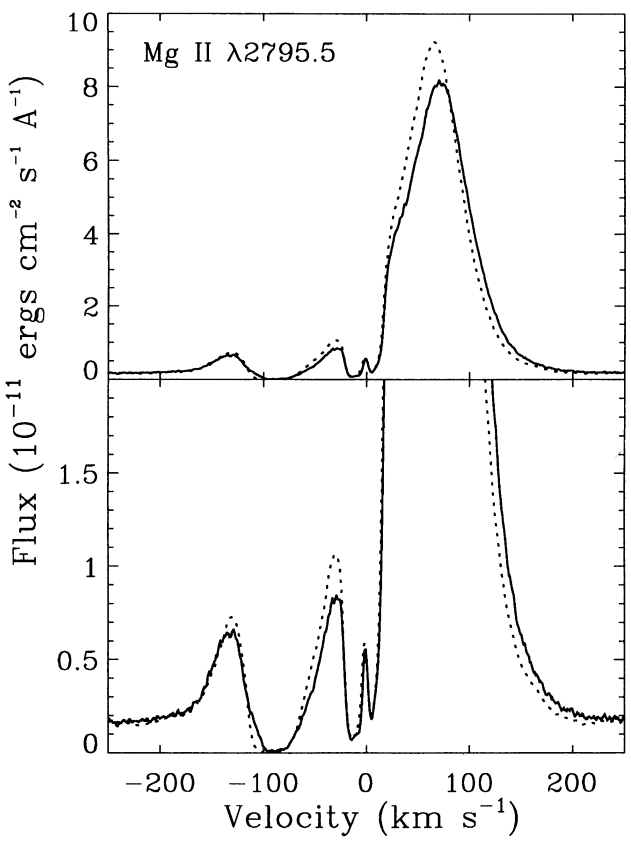

FIG. 4.—A comparison of the Mg II *k* line profiles taken with different instrumental configurations at different times. The dashed line is the post-COSTAR SSA observation degraded to match the resolution of the pre-COSTAR LSA observation (*solid line*). The velocity scale is in the stellar rest frame. The bottom frame is enlarged to show the profile differences near the ISM and wind features.

2.2. *The G200M Spectrum*

The G200M spectrum (Fig. 2) shows the complex absorption line spectrum underlying the diagnostic emission lines of S I UV1, Si III], and C III]. It is clear that a detailed analysis of these lines requires a realistic continuum model. We considered three approaches to obtain a continuum model for the G200M spectral region.

1. *Modified radiative equilibrium model.*—We constructed a radiative equilibrium (RE) model for α TrA using the TLUSTY code of Hubeny (1988). It showed that the continuum near 1900 Å forms ($\tau_{cont} \sim \frac{2}{3}$) above the temperature minimum of semiempirical models (Harper 1992a). The radiative equilibrium model (no nonradiative heating) consequently predicts fluxes that are smaller than observed. We then added the model chromosphere from Harper (1992a) to the model RE photosphere to schematically represent the chromospheric temperature rise. The ionization balance of the neutral and singly ionized metals was computed with non-LTE photoionization rates.

2. *Pure absorption model.*—The spectrum of a multislab chromspheric model (Harper 1992a) illuminated at the base with a blackbody continuum was computed assuming pure absorption. The first two ionization stages of all elements up to Ni were included, and the ionization of the neutrals was treated with a schematic photoionization rate. The line opacity was computed from all levels that share the same parity as the ground state of the respective ion, and the relative populations were assumed to be in a Boltzmann distribution characteristic of the temperature at that column density.

3. *Theoretical model of Capella.*—For this model we took the radiative equilibrium photospheric model of Capella described in Linsky et al. (1995) and convolved it with a rotational broadening of $v \sin i = 2$ km s^{-1} and then smoothed the spectrum with the G200M PSF. The atmosphere was then scaled to the continuum level shown in Figure 2.

2.2.1. *Comparison of Continuum Models*

A visual inspection of the three different models showed that they are closer to each other than to the observations, with the model for Capella providing marginally the best agreement. The similarities between these essentially absorption models of gas in the photosphere and lower chromosphere allow us to identify several regions where there is little line opacity: when such regions are convolved with the appropriate PSF the resulting continuum level is close to the intrinsic continuum level. This allows us to identify the stellar continuum level in our spectrum. Near λ1882.6, λ1894.5, λ1896.8, λ1907.1, and

λ1916.4, the flux lies within 5% of the intrinsic continuum. Figure 2 shows that these continuum windows are very close to the maximum level of the observed continuum except at λ1916.4. If the continuous opacity varies slowly over this region so that the same depth in the atmosphere is sampled, then the continuum gradient implies a temperature $T_e > 5000$ K consistent with the estimated chromospheric temperature at $\tau_{cont} \simeq \frac{2}{3}$. The radiative equilibrium model with the chromospheric temperature rise shows that the Al I photoionization edge at 2076 Å is expected to dominate the opacity at this wavelength, but the computed models predicted fluxes that were too small. It is not clear whether this is due to the assumption of a one-dimensional homogeneous atmosphere, or to some non-LTE physics not included in the calculations. The absolute intensity gives an indication of the departure coefficient of the dominant source of opacity and the filling factor of the warmest material, since the continuous emission is from a thermal process and the Planck function at these wavelengths is a very strong function of T_e. Detailed models of the continuum may provide strong diagnostics for chromospheric inhomogeneities, when combined with traditional resonance line diagnostics. The importance of making realistic models for the photosphere *and* chromospheres of evolved late-type stars cannot be overstated since the uncertainties in the emission-line parameters are *dominated* by the uncertainties in the structure of the continuum. We will pursue the construction of more realistic photospheric/chromospheric models in a future paper, but for now we adopt the theoretical model of Capella to illustrate this point.

The similarity of the 1900 Å energy distribution of α TrA to that of the photosphere of a much hotter star (i.e., the G0 III star of Capella) is consistent with the *IUE* study by Ayres (1985). He compared the far-UV energy distribution of α TrA with those of red giants of similar $(B-V)$ color, like α Boo (K1 III) and α Tau (K5 III), and noted that the 1900 Å spectrum of the archetype hybrid appeared to be significantly bluer than that of the other red giants. Ayres interpreted the enhanced continuum as resulting from a previously unrecognized F dwarf companion and concluded that some of the unusual aspects of the hybrid-chromosphere phenomenon might be due to the binary nature of the systems. Subsequently, however, Burton (1991) showed that UV continuum excesses, relative to *IRAS* 12 μm fluxes, are common among the hybrid stars and appear to be well correlated with activity indices, like R_{hk} and $R_{C\,IV}$. Thus, the excesses very likely are due to a significant contribution to the 1900 Å continuum emission from the higher temperature chromospheres themselves, rather than due to a proliferation of warm stellar companions. The effect is more pronounced in the bright giants and supergiants owing to the general extension of their photospheres in mass column density, which favors high-altitude formation of the Si I and Al I continua.

2.2.2. *Emission Line Parameters*

We considered two ways of measuring the line fluxes, wavelengths, and line widths: first with a flat continuum model, and second with the model continuum flux adopted above, which is probably more realistic. We applied weighted least-squares Gaussian fits, assuming that the profiles are intrinsically Doppler broadened. We rotationally broadened the model Gaussian profiles assuming a nominal value of $v \sin i = 2.0$ km s^{-1} and then convolved the profiles with the PSF for the G200M grating described in Gilliland & Hulbert (1993). The fits are insensitive to the value of $v \sin i$ so long as it is small compared to the intrinsic broadening. Since the Si III] and C III] lines are expected to be optically thin and the S I lines have low optical depths (see § 2.2.3), Gaussian profiles should be good approximations to the intrinsic line shapes. The results are given in Table 2, where the quoted values of FWHM are those of the *intrinsic* emission line (i.e., before convolution with the PSF), and the velocities given are in the stellar rest frame. The errors are estimated using the procedures outlined in Lenz & Ayres (1992), which assume a noiseless continuum subtraction. These errors also do not include any estimate of the error in the PSF. The result given in Table 2 demonstrate that inaccuracies in the continuum model dominate the true uncertainties in the line profile parameters.

2.2.3. S I *UV1*

The two sulfur UV1 emission lines at λ1900.268 and λ1914.698 have well-determined laboratory wavelengths that are thought to be accurate to 0.13 km s^{-1} (Kaufman 1982). These lines are formed in the chromosphere and can be used as velocity diagnostics. In the line profile fits (Table 2) we fixed the separation of the line centers according to the laboratory separation and assumed the same Doppler width. We find that the S I lines show no Doppler shift relative to the photosphere. Previous *IUE* measurements of the fluxes of the S I UV1 lines are quite uncertain because of the poorly characterized underlying continuum flux and the low signal-to-noise ratio of the data. Hartmann et al. (1985) found the ratio $F(1900.3)/F(1914.7) = 1.5(\pm \sim 0.45)$ in both low- and high-resolution *IUE* spectra of α TrA. The GHRS ratio is $F(1900.3)/F(1914.7) = 2.3 \pm 0.2$. The GHRS flux of the stronger UV1 line λ1900.3 is similar to that measured by Hartmann et al. (1985), while the λ1914.7 line is weaker. The width of the lines [assuming $V_{Dopp} = \mathrm{FWHM}/(2\sqrt{\ln 2})$] suggests turbulent

TABLE 2

EMISSION-LINE INFORMATION FROM THE G200M SPECTRUM

Ion	Rest Wavelength (Å)	ΔV (km s^{-1})	Flux (ergs cm^{-2} s^{-1})	FWHM (Å)
Flat continuum:				
S I	1900.286	-0.2 ± 0.3	$(1.74 \pm 0.07) \times 10^{-13}$	0.138 ± 0.008
S I	1914.698	-0.2 ± 0.7	$(7.0 \pm 0.5) \times 10^{-14}$	0.138 ± 0.005
C III]	1908.734	$+5.4 \pm 0.7$	$(2.23 \pm 0.05) \times 10^{-13}$	0.46 ± 0.01
Si III]	1892.030	$+6.4 \pm 0.7$	$(2.70 \pm 0.05) \times 10^{-13}$	0.58 ± 0.01
Model continuum:				
S I	1900.286	-0.0 ± 0.3	$(1.95 \pm 0.07) \times 10^{-13}$	0.150 ± 0.005
S I	1914.698	-0.0 ± 0.3	$(8.5 \pm 0.05) \times 10^{-14}$	0.150 ± 0.008
C III]	1908.734	$+5.4 \pm 0.7$	$(2.24 \pm 0.05) \times 10^{-13}$	0.48 ± 0.01
Si III]	1892.030	$+3.2 \pm 0.7$	$(3.07 \pm 0.05) \times 10^{-13}$	0.61 ± 0.01

motions of $V_{\rm Dopp} \leq 14$ km s^{-1} (depending on the magnitude of $v \sin i$), which is less than the value found from *IUE* observations of the C II] ($V_{\rm Dopp} \sim 30$ km s^{-1}) by Hartmann et al. (1985) which might indicate an increase of turbulence with height.

The formation of the S I UV1 lines in evolved late-type stars has been studied by Judge (1988) who found that these lines are formed by radiative recombination to the ^5P series of terms following photoionization by UV continua at $\lambda < 1197$. The two lines share a common upper level and can be used to infer the neutral sulfur column in the line-forming region. Here we follow the method described by Jordan (1967). We assume that the lines are formed above their thermalization depth and that those S I UV1 photons that do not escape from the atmosphere instead scatter in the line. Multiple scattering will enhance the weaker line relative to the stronger line and the number of scatterings is proportional to the optical depth in the lines. We calculate the probability of escape by assuming a plane-parallel slab model and a Doppler atomic emission profile. Since the lines are formed by radiative recombination, the flux is proportional to the emission measure $\int n_e n_{\rm S\,II}\, dh$ with a weak temperature dependence. Since the dominant fraction of the integral comes from the chromosphere, a slab model should be a reasonable representation (within the context of a homogeneous chromosphere).

We assume for now that all photons emitted toward the photosphere are scattered rather than thermalized, but the following remains valid if a given fraction (the same for both lines) of the photons scattered are thermalized. The escape probability in the forward direction is computed numerically by summing the escape probability for each frequency and angle. The oscillator strengths of these lines are not accurately determined, and we adopt $f_{\rm abs}(1900.3\ \text{Å}) = 3.573 \times 10^{-5}$ and $f_{\rm abs}(1914.7\ \text{Å}) = 1.740 \times 10^{-5}$ (Morton 1991). Assuming $T_e \sim$ 6000 K for the temperature of formation, we compute the flux ratio as a function of the S I λ1900.3 line center optical depth which is shown in Figure 5. Since the ratio falls rapidly at radial optical depths close to unity, changes in the flux ratio would *not* necessarily require significant changes in the chromospheric structure. Indeed, in the best-studied evolved late-type stars the flux ratio appears to be greater than unity but less than the optically thin limit. The line ratio is therefore a *sensitive* diagnostic of changes in the ionization balance of sulfur and hence the UV radiation field. Adopting a solar sulfur abundance [$A(S_\odot) = 1.62 \times 10^{-5}$; Anders & Grevesse 1989] the mass-column density corresponding to $\tau_{1900} = 0.3$ is 5.4×10^{-3} g cm^{-2}, which corresponds to a temperature of $T_e \sim 5300$ K in the model of Harper (1992a).

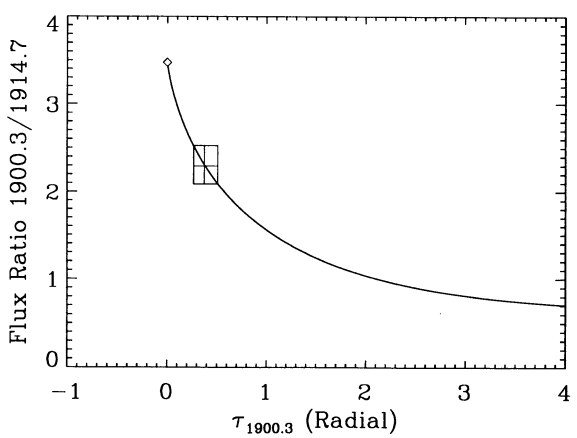

FIG. 5.—The S I λ1900.3/λ1914.7 flux ratio of as a function of the radial line center optical depth of the λ1900.3 line. The box indicates the estimated errors in the line ratio from the flux uncertainties. The diamond represents the optically thin limit.

The ratio of the S I UV1 fluxes to the inferred S I column density, together with an estimate of the electron density (e.g., from the C II] 2325 Å multiplet), may potentially permit us to estimate the S II/S I ionization balance. Judge (1988) found that if charge exchange does not dominate the ionization balance, then the dominant recombination pathways are radiative and low-temperature dielectronic recombination. Unfortunately, these atomic data are also uncertain and the charge exchange rates of Butler & Dalgarno (1980) may be overestimates (Judge 1988). Improved atomic data are required before this diagnostic can be utilized.

2.2.4. Si III] *and* C III]

These optically thin emission lines are formed at transition region temperatures and show much larger Doppler broadening than the S I lines. Comparison of the intersystem C III] λ1908.734 and Si III] λ1892.030 line fluxes with those of the corresponding electric quadrupole lines at [C III] λ1906.680 and [Si III] λ1882.710 can provide estimates of the electron density. We see no clear evidence for the quadrupole emission lines in the structured continuum, but we can estimate upper limits to their fluxes. We assume that they have an intrinsic Doppler-broadened profile with widths determined from the intersystem lines. We note that the [Si III] line lies on a continuum window, while the [C III] line lies near the edge of one. Intrinsic profiles were computed and co-added to the rather uncertain continuum model and then smoothed with the G200M PSF. We adjusted the estimated fluxes of the quadrupole lines until they appeared to exceed the maximum expected continuum level. We rather subjectively adopt those values as the upper limit to the quadrupole fluxes.

We determine the lower limit to n_e from the observed lower-limit of the Si III]/[Si III] flux ratio of $\geq$30. We solve the statistical equilibrium equations for a Si III model atom with the first 20 fine-structure levels using the radiative rates computed by Nussbaumer (1986), except for the $3s^2\,{}^1S$–$3s3p\,{}^3P$ transitions, for which we adopt the results of Ojha, Keenan, & Hibbert (1988). Their computed radiative rate for the intersystem line agrees well with the observed value of Kwong et al. (1983). The electron collision rates are taken from Dufton & Kingston (1989). Adopting a temperature of formation of $T_e \simeq$ 50,000 K, we find $n_e \geq 3 \times 10^6$ cm^{-3}.

For C III we adopt a model atom with the first 10 fine-structure levels and the transition probabilities of Nussbaumer & Storey (1978) supplemented by the calculations of Froese-Fischer (1994) and Idrees & Das (1989). Note that the adopted A-value of the intersystem line (103 s^{-1} from Froese-Fischer) agrees with the calculations of Fleming, Hibbert, & Stafford (1994) but is smaller than the measurement of Kwong et al. (1993) (121 s^{-1}). We adopt the electron collision strengths of Berrington (1985) and Berrington et al. (1985), and for the proton rates between the $2s2p\,{}^3P$ levels we adopt the rates of Doyle (1987). We adopt a formation temperature of 70,000 K, and from the lower limit of the C III]/[C III] flux ratio of $\geq$9, we find that $n_e \geq 7 \times 10^5$ cm^{-3}.

The Si III] line is asymmetric and this is likely due to the shape of the underlying continuum, which gives the line an apparently bright red wing. The velocity centroids for these

optically thin lines given in Table 2 are uncertain due to the uncertainty in the continuum model, but they suggest the lines are redshifted toward the photosphere and not blueshifted, as would be expected if the lines formed in the outflow of a stellar wind. Higher resolution observations, more detailed continuum modeling, and accurate quadrupole line strengths are required to further constrain these diagnostics.

2.3. *The G160M spectrum*

The G160M spectrum (Figure 2) shows the C IV doublet at $\lambda\lambda$1548.202 and 1550.774. These lines share the common ground state lower level. The C IV lines are *asymmetric* and differ in shape from each other, possibly due to coincident emission and/or overlying absorption features. The integrated fluxes of the two lines are $F_{1548.202} = (3.00 \pm 0.05) \times 10^{-13}$ ergs cm^{-2} s^{-1} and $F_{1550.774} = (1.73 \pm 0.04) \times 10^{-13}$ ergs cm^{-2} s^{-1}. These fluxes are similar to those measured from *IUE* spectra (Hartmann et al. 1981; Hartmann et al. 1985). The C IV line profiles are broad, FWHM$_{1548.202} \simeq 164$ km s^{-1} and FWHM$_{1550.774} \simeq 133$ km s^{-1} (Linsky, Wood & Andrulis 1994), with the more opaque line being wider, possibly owing to opacity broadening. There are several other lines visible in Figure 2, but we defer the detailed analysis of the spectral region to a future paper.

3. THE INTERSTELLAR ABSORPTION FEATURES

There is considerable evidence that the Sun lies inside a small cloud of warm neutral gas ($T_e \simeq 7000$ K; Linsky et al. 1993). Table 3 lists the upwind direction velocity vectors for several models of this cloud and the heliocentric line-of-sight components of these vectors in the direction of α TrA. The model of Bertaux et al. (1985) labeled VLISM and that of Crutcher (1982) have single velocity components. The model of Lallement & Bertin (1992) is a two-component model, with components V^G and V^{AG} applying to stars that are located roughly in the Galactic center and anti-Galactic center directions, respectively. The four clouds (A, O, P, and I) proposed by Lallement, Vidal-Madjar, & Ferlet (1986) also are listed in Table 3.

The Mg II lines of α TrA exhibit two clear interstellar absorption components—one with a heliocentric velocity of -17.3 km s^{-1} and the other with a velocity of $+3.4$ km s^{-1}. As Table 3 shows, the V^{AG} and V^G vectors of Lallement & Bertin (1992) are the best matches for the blueshifted component, and Figure 3 of their paper indicates that α TrA should be in the direction of the V^G cloud. With a Galactic longitude of $l^{II} = 332°$ and a Galactic latitude of $b^{II} = -15°$, the α TrA line-of-sight flow velocity due to V^G should be -16.7 km s^{-1}. However, the component centered at $+3.4$ km s^{-1} does not admit to such a ready explanation. Lallement et al. (1986) find an additional interstellar absorption component at $+7.8$ km s^{-1} toward the star α Cru located about 27° from α TrA. Because that component is not seen toward other stars, they could not determine the associated flow vector. Nonetheless that cloud might well be responsible for the $+3.4$ km s^{-1} feature seen in the α TrA spectrum.

TABLE 3

INTERSTELLAR LINE-OF-SIGHT VELOCITIES TOWARD α TRIANGULI AUSTRALIS

Velocity Vectors	Modulus (km s^{-1})	l^{II}	b^{II}	v_{los} (km s^{-1})	Reference
Crutcher.....	28	205°	−10°	−10.6	1
VLISM.....	20	184	−16	−12.2	2
V^G.....	29.4	185	−21	−16.7	3
V^{AG}.....	25.7	186	−16	−15.0	3
A.....	25	213	−19	−5.1	4
O.....	22	199	−15	−9.5	4
P.....	35	192	−14	−18.6	4
I.....	29	192	+19	−19.3	4
α TrA.....	...	322	−15	...	
α Cru.....	...	300	−0	+7.8[a]	4

[a] This velocity is for the line of sight toward α Cru, not α TrA.

REFERENCES.—(1) Crutcher 1982; (2) Bertaux et al. 1985; (3) Lallement & Bertin 1992; (4) Lallement et al. 1986.

To model the ISM features we have used our post-COSTAR Mg II spectrum obtained with the SSA, as this spectrum has significantly higher resolution than the pre-COSTAR LSA spectrum. For the ISM, we assume a magnesium abundance (assumed to be entirely Mg II) of 1/10 of solar ($A_{Mg\odot} = 3.8 \times 10^{-5}$; Anders & Grevesse 1989) to account for depletion (i.e., the same depletion as observed by Linsky et al. 1993 for the line of sight to Capella). We modeled each of the two observed ISM features individually, with its own Doppler parameter b (km s^{-1}), neutral hydrogen column $N_{H\,I}$ (cm^{-2}), and heliocentric velocity (V_{rad}). The best fits are illustrated in Figure 6. Fourth-degree polynomial fits, shown as dotted lines in Figure 6, have been used to estimate the intrinsic stellar (plus wind) Mg II line profiles. The form of the adopted intrinsic

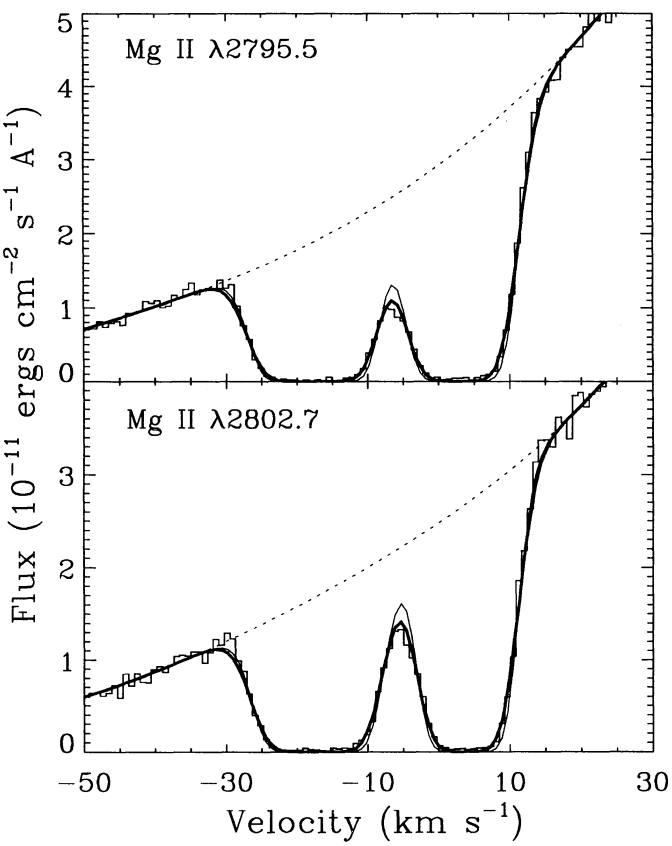

FIG. 6.—The ISM absorption features observed in the two Mg II lines. The data are shown in histogram form. Our best fit to the ISM lines is also shown (see Table 4 for fit parameters). Fourth-degree polynomial fits (*dotted lines*) have been used to estimate the intrinsic stellar (plus wind) Mg II line profiles in the spectral regions contaminated by the ISM absorption. The absorption profile of the two interstellar absorption components is shown as a narrow solid line, and the convolution of the profile with the instrumental profile is shown as a thick solid line.

TABLE 4

FIT PARAMETERS FOR THE TWO INTERSTELLAR COMPONENTS

	V_{rad} (km s^{-1})	$\log_{10}[N_{H\,I}(cm^{-2})]$	b (km s^{-1})
Mg II k.....	−17.45	18.99	5.57
	+3.00	18.78	5.05
Mg II h.....	−17.13	19.24	5.59
	+3.85	19.02	4.45
Mean	−17.3 ± 1.5	19.1 ± 0.2	5.6 ± 0.4
	+3.4 ± 1.5	18.9 ± 0.2	4.8 ± 0.4

profile is supported by the results of our simulations presented in § 4.2.2. For a given set of parameters, the profiles for the two interstellar absorption components were computed and then convolved with the echelle-B SSA instrumental profile (Gilliland & Hulbert 1993). In Figure 6, the absorption profile of the two ISM components is shown as a narrow solid line, and the convolution with the instrumental profile is shown as a thick solid line. The derived parameters for the two Mg II lines are listed in Table 4, together with the means of the two fits. The uncertainty in the measured velocity is assumed to be the same as for typical echelle spectra (see Linsky et al. 1993). The average parameters for the best fits shown in Figure 6 give Doppler broadening parameters of the blueshifted (−17.3 km s^{-1}) and redshifted (+3.4 km s^{-1}) ISM components of 5.6 and 4.8 km s^{-1} and logarithmic hydrogen column densities of 19.1 and 18.9, respectively. However, because the lines are on the flat part of the curve of growth, there is an interplay between the Doppler broadening parameter and the inferred column density. Therefore, the uncertainties are fairly large. We performed the analysis using the pre-COSTAR LSA Mg II h and k line profiles, and the results were similar to those given above but with slightly larger column densities.

The total neutral hydrogen column of our best fit, $N_{H\,I} = 2 \times 10^{19}$ cm^{-2}, is consistent with the estimate found by Brown et al. (1991) ($N_{H\,I} = 5 \times 10^{19}$ cm^{-2}; based on Lyα fitting) and that reported by Kashyap et al. (1994) (3–6 × 10^{19} cm^{-2}; derived from *ROSAT* PSPC spectrum), considering the uncertainties inherent in our fitting procedure and the unknown depletion in that line of sight.

4. THE WIND ABSORPTION FEATURE

As a first step toward understanding the Mg II h and k line profiles, we have constructed simple models for the wind scattering environment. In our physical picture of a typical stellar chromospheric/wind, optically thick but *effectively thin* emission lines (see Judge 1990) form in the denser layers of the chromosphere where the emission measures are largest. The Mg II line photons then scatter in more tenuous outer regions where the density stratification is described by the momentum and continuity equations. The scattering zone modifies the emission profile but conserves line photons.

4.1. *Description of the Wind Model*

With the above picture in mind, we simulate the wind scattering of the Mg II h and k lines with a two-level atom in an expanding spherically symmetric atmosphere. Instead of modeling the full chromospheric structure, which is a very complex task, we prescribe a specific intensity profile, $I_{\Delta\nu}(\mu)$, which is isotropic and incident on the inner boundary at the base of the wind, at a height in the chromosphere ($R = 1.04R_*$, $R_* = 97\ R_\odot$) where we anticipate that the wind velocity, V_{wind}, is still less than the characteristic turbulence motions, V_{turb}. Here $\cos^{-1}\mu$ is the angle of the ray to the radial direction, and $\Delta\nu$ is the frequency offset from line center. The specific intensity profile is assumed to be symmetrical (in wavelength about line center) in the rest frame of the star, i.e., $I_{+\Delta\nu} = I_{-\Delta\nu}$. Our ignorance of the actual chromospheric structure is thus confined to the adopted intensity profile at the base of the wind. The geometry and quadrature schemes of the transfer problem are those described in Harper (1994). We seek a self-consistent solution to the equations of statistical equilibrium and radiative transfer for the two-level model atom. We solve the radiative transfer equation with a standard Feautrier method and converge the solutions using an accelerated lambda iteration (ALI) scheme combined with Ng acceleration (Ng 1974) We choose the input intensity profile such that in the absence of an expanding optically thick wind, the observed flux profile in the far red wing is recovered. Because the photons are scattered rather than absorbed, the input intensity is tightly constrained by the observed total flux. We also assume there is no incident radiation on the outer boundary of the wind. We assume complete redistribution of the photons over the emission profile after each scattering and a constant microturbulence V_{turb}. Since the radiation field in the modeled region is decoupled from the *thermal* structure of the wind (except through ionization), we can adopt an isothermal wind and constant continuous opacity. Our knowledge of the intrinsic intensity profile is least near line center, which is also where the ISM absorption is strongest, so the following model provides information only on the portion of the line profile where $\Delta V < -30$ km s^{-1} (where $\Delta V = 0$ km s^{-1} is line center). For the velocity fields we assume that the wind speed represents the mean outward motion of turbulent elements corresponding to the mass flux and that the turbulent velocity is some root mean-squared average of the distribution of velocities about the mean outward flow.

In the absence of a physical model for the mass loss from evolved late-type stars, we adopt an exponential density distribution with a density scale height of $H = V_{turb}^2/(2g_*)$ at the base of the flow, combined farther out with the density distribution from a constant power-law, i.e.,

$$\rho(R) = \frac{\dot{M}}{4\pi R^2 V(R)} = \frac{\dot{M}}{4\pi R^2 V_\infty}\left(1 - \frac{R_*}{R}\right)^{-\beta}, \qquad (1)$$

where V_∞ is the terminal velocity, $\dot{M}$ is the mass-loss rate, and β is the velocity power-law parameter. In the region where the computed models are sensitive to the velocity and density distribution, these are determined by the power-law relationship. For the purposes of modeling, the velocity $V(R)$ is then given by the density distribution and the equation of continuity together with the assumption that the flow is time independent above the reference radius. We assume that the photospheric Mg II abundance is $A_{Mg\,II} = 5.8 \times 10^{-5}$ ($A_{Mg_\odot} = 3.8 \times 10^{-5}$, Anders & Grevesse 1989) based on the analysis of α TrA by Kovács (1983).

The input parameters of the models are: (1) the power-law parameter β, (2) the mass-loss rate $\dot{M}$, (3) the terminal velocity $V(\infty)$, (4) the turbulent velocity V_{turb}, and (5) the incident specific intensity profile. Once we have found the model, which, within the uncertainties, best matches the blue halves of both the Mg II h and k profiles, we analyze the resulting velocity distribution with numerical solutions to a momentum equation.

4.2. *Results from Model Calculations*

4.2.1. *Flux Profiles*

Figures 7 and 8 show our best fits to the observed LSA line profiles for the assumed input intensity profiles. These solutions are not unique since the calculations are relatively insensitive to the wind acceleration rate. The adopted intensity profiles are shown in Figures 7 and 8 as the flux profiles that would have been observed in the absence of any wind scattering. The wind model shown has the parameters $\dot{M} = 1.8 \times 10^{-10}\ M_\odot\ \mathrm{yr}^{-1}$, $V(\infty) = 100\ \mathrm{km\ s}^{-1}$, $V_{\mathrm{turb}} = 24\ \mathrm{km\ s}^{-1}$, and $\beta = 1.0$. At the wind flux minima the models are not quite as dark as the observations, and the models also fail to reproduce the profile in the far blue wing. To match the far blue wings either a multicomponent wind model is needed, or one must assume that the initial intensity profile is intrinsically redshifted rather than centered on the photospheric velocity as we have assumed.

Perturbations of the terminal and turbulent velocities indicate that for this set of model assumptions $V(\infty) = 100 \pm 5\ \mathrm{km\ s}^{-1}$ and $V_{\mathrm{turb}} = 24 \pm 5\ \mathrm{km\ s}^{-1}$, with the additional constraint that $V(\infty) + V_{\mathrm{turb}} = 124 \pm 5\ \mathrm{km\ s}^{-1}$. For a fixed value of β we find $\dot{M} = (1.8 \pm 0.3) \times 10^{-10}\ M_\odot\ \mathrm{yr}^{-1}$. Because these models are nonunique, the given range of parameter space must be regarded as a lower limit to the true uncertainty.

Figure 9 shows our best fit to the Mg II *k* line post-COSTAR, SSA observation. This wind model has the parameters $\dot{M} = 1.6 \times 10^{-10}\ M_\odot\ \mathrm{yr}^{-1}$, $V(\infty) = 104\ \mathrm{km\ s}^{-1}$, $V_{\mathrm{turb}} = 19\ \mathrm{km\ s}^{-1}$, and $\beta = 1.0$. The additional constraint in this case is tighter, $V(\infty) + V_{\mathrm{turb}} = 123 \pm 3\ \mathrm{km\ s}^{-1}$, because the observed profile is symmetric in the photospheric rest frame and is more reliably modeled with a single wind component. Again, the wind model is not as dark as the observations at the wind minimum feature, but the computed far blue-wing shows an acceptable fit. Although the observed pre- and post-COSTAR profiles are noticeably different, the difference in the wind models is small compared to the likely uncertainties in the models. Small perturbations to the model parameters lead to significant changes in the computed profiles. The higher value of V_{turb} required to fit the LSA observation is due to the additional attenuation required to model a broader specific intensity profile. The shape of the mismatch of the wind model for both the LSA Mg II *h* and *k* line profiles suggests but does not prove that the intrinsic stellar profile has been shifted in the stellar rest frame. These wind models predict some attenuation of the emission profile beyond the maximum wind velocity due to the finite velocity dispersion of the wind. The SSA line profile, near the wind flux minimum, shows steeper flux gradients (when degraded to the pre-COSTAR LSA resolution) suggestive of a lower velocity dispersion in the wind during this observation. This is consistent with the symmetry of the Mg II *k* profile in the SSA observation. The wind crossing time from $2R_*$ to $15R_*$, where the Mg II *h* line has its maximum scattering radius ($\tau_{\mathrm{Mg\ II}\ h} = 1$) is approximately 90 days which is roughly the timescale for wind profile variability as determined from *IUE* data (see Hartmann et al. 1985), so it is quite possible that there are multiple wind components present in the Mg II resonance line scattering region.

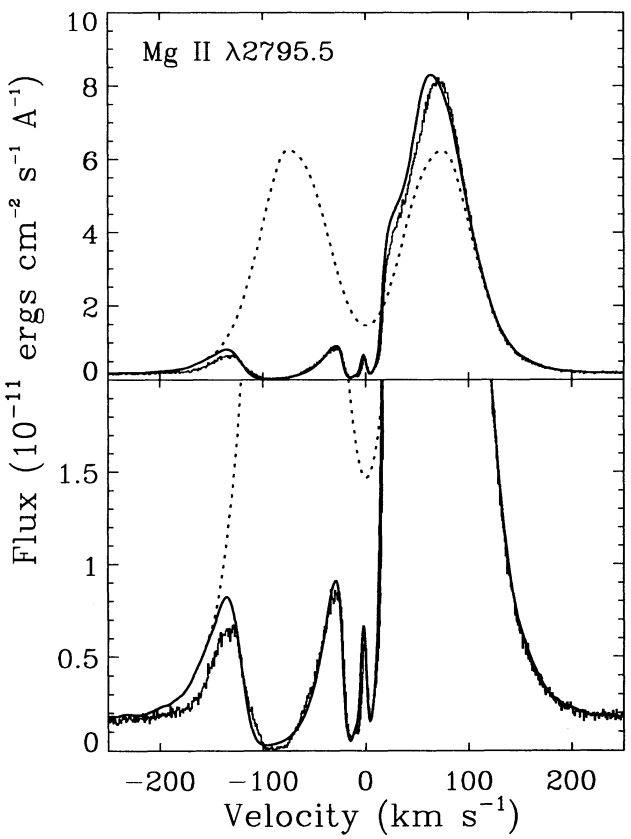

FIG. 7.—The observed pre-COSTAR LSA (*histogram*) and computed (*solid line*) Mg II *k* line flux profile for α TrA. Also shown (*dotted line*) are the flux profiles that correspond to the assumed intensity profiles in the absence of any overlying wind or interstellar opacity. The bottom frame is an enlargement to show the model fit near the wind and ISM features. The velocity scale is in the stellar rest frame.

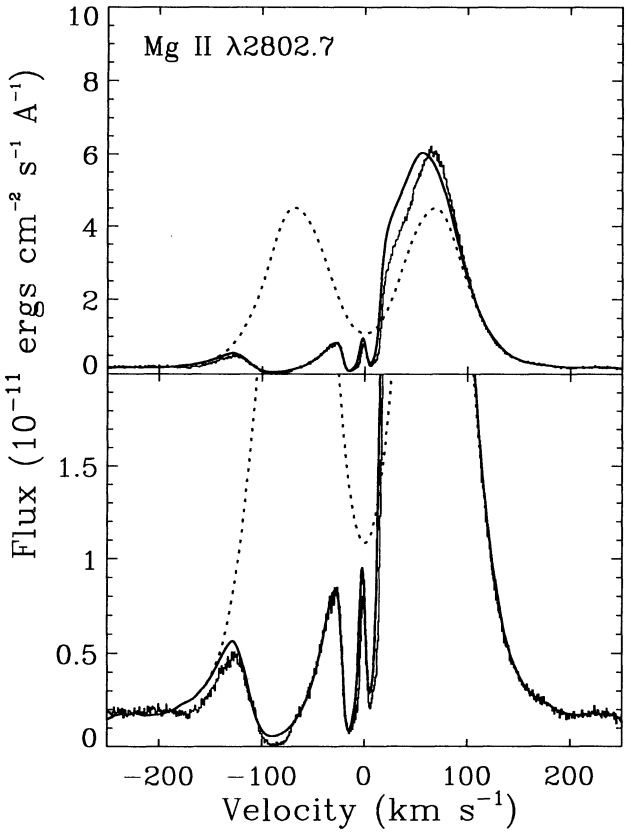

FIG. 8.—Same as Fig. 7 except for the Mg II *h* line

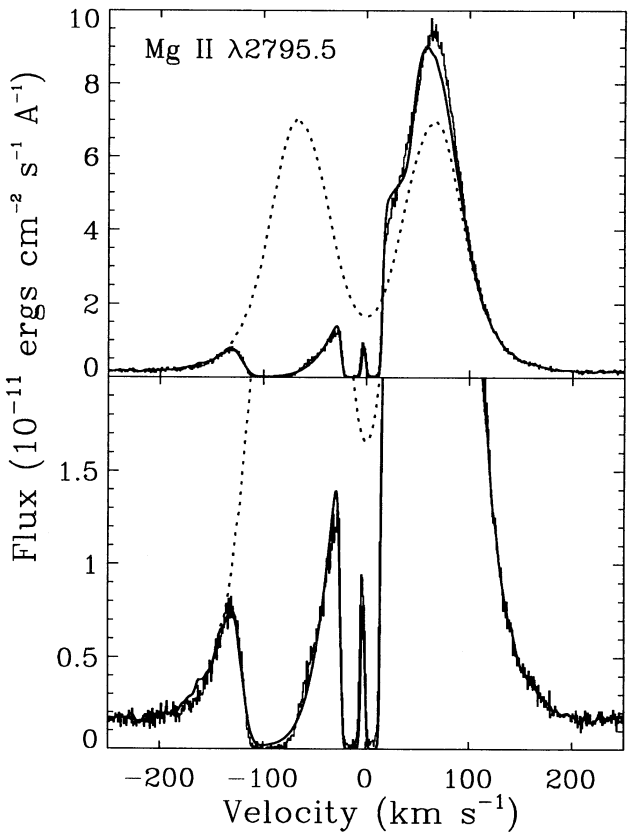

FIG. 9.—The observed post-COSTAR SSA (*histogram*) and computed (*solid line*) Mg II *k* line flux profile for α TrA. Also shown (*dotted line*) are the flux profiles that correspond to the assumed intensity profiles in the absence of any overlying wind or interstellar opacity. The lower frame is an enlargement to show the model fit near the wind and ISM features. The velocity scale is in the stellar rest frame.

The sensitivity of the calculated profiles to the mass-loss rate and power-law can be seen from the following arguments. The maximum opacity in the wind occurs near -95 km s^{-1}, which is well within a Doppler width of the terminal velocity (100 km s^{-1}). The velocity gradient had decreased significantly at these radii (R), and satisfies the condition that

$$V_{\rm turb}(R) \gg R\left(\frac{dV}{dR}\right)_R , \qquad (2)$$

i.e., the changes in the wind velocity from radius, R, to infinity are small compared to the Doppler width. We can then neglect the effect of the wind velocity gradient on the optical depth to a radius R, since its variation is small compared to the velocity dispersion. The line optical depth can then be approximated by integrating the radial opacity ($\propto 1/R^2$). The line opacity for a Doppler-dominated absorption profile is inversely proportional to the Doppler width. The optical depth in the wind where it has reached a significant fraction of its terminal velocity is then proportional to

$$\tau \propto \int_R^\infty \rho\phi\, dR \propto \frac{\dot{M}}{V_{\rm turb}\, V(\infty) R} , \qquad (3)$$

where R is the radial distance at which this velocity is reached, $\phi \sim V_{\rm turb}^{-1}$ is the Doppler line profile, and ρ is given in equation (1). If the power-law parameter of the wind β could be constrained by some other diagnostic and Mg II is the dominant ionization state, then the required mass-loss rate would be inversely proportional to the product of the terminal and turbulent velocity. The value of R can be derived from the assumed form of the velocity law, but we have no knowledge of the wind acceleration that determines the radial distance in equation (3). The model for α TrA assumes $\beta = 1.0$, but numerically we find, very approximately, that mass-loss rates satisfying $\dot{M} \sim \beta \times 1.8 \times 10^{-10}\ M_\odot\ {\rm yr}^{-1}$ are potentially able to provide sufficient wind opacity. Values of $\beta < 0.3$ lead to excessive emission near $V = -40$ km s^{-1} due to an absence of overlying opacity resulting from the velocity shear. If instead we have adopted $\beta = 2.5$ or 3.5, as found in the most recent wind scattering calculations for ζ Aur systems (Baade 1992; Kirsh & Baade 1994) *and* had obtained sensible fits to the profiles, then the radial distance in equation (3) would increase by a factor of 3. This would imply that the mass-loss rate is a factor of 3 to 4 larger than in the above model. As we have assumed that Mg II is the dominant ionization stage of magnesium, the mass-loss rates found for the small values of β represent a firm lower limit to the actual mass-loss rate from α TrA if the stellar radius is close to $R_* = 97\ R_\odot$. Figure 10 shows the results of calculations for the SSA Mg II *k* line profile for three different assumed stellar radii, $R_* = 75$, 97, and 125 $R_\odot$. For a given mass-loss rate the star with a smaller radius has a higher mass-flux (per unit area) and produces a deeper absorption trough. This figure shows that the uncertainty in the basic stellar parameters can lead to systematic uncertainties in wind

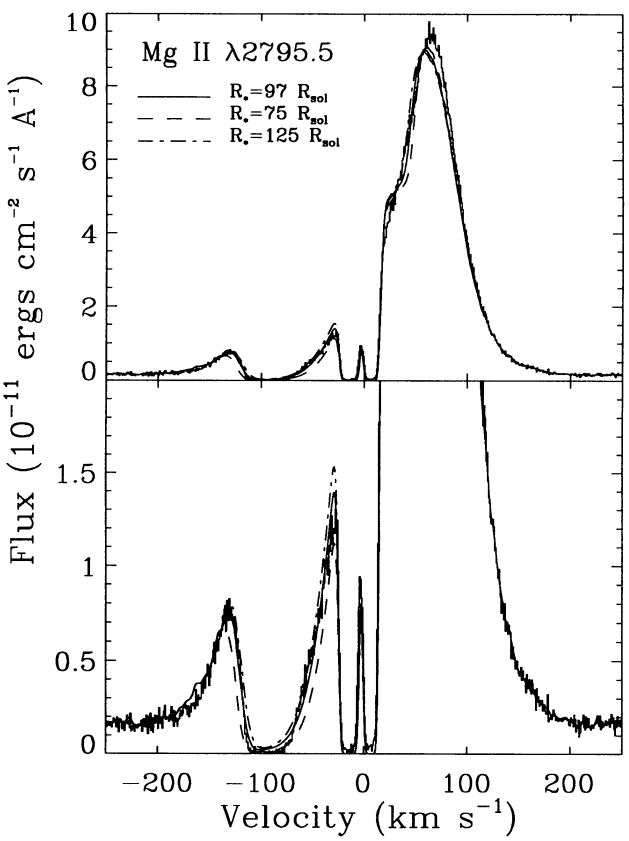

FIG. 10.—These model profiles for the Mg II *k* line based on the same $\dot{M}$, $V_{\rm turb}$, and β as used to fit the SSA observation, with three different stellar radii, $R_* = 75$, 97, 125 $R_\odot$. This figure shows that the uncertainty in stellar parameters will lead to a systematic uncertainty in the wind model parameters.

models. Stellar parallaxes from the *HIPPARCOS* mission will greatly aid the interpretation of the stellar spectra.

The emission feature at $V = -40$ km s^{-1} results from a combination of the scattering of blue photons toward line center and attenuation by the ISM. This part of the line profile also reflects the dynamically important region where $V_{\rm wind} \sim V_{\rm turb}$. This region is best probed by optically thick emission lines like O I 1306.03 Å and 1304.86 Å, which have little profile contamination from ISM scattering owing to their excited lower levels. Alternatively, stars with large negative radial velocities will have their ISM absorption superposed on the red emission peak. The differences between the computed and observed profiles above the red peak are in part due to the assumption of complete frequency redistribution, the assumed intensity profile, and the adopted form of wind acceleration.

4.2.2. *Projection of the Sky Intensity and the ISM Feature*

One of the most noticeable results in our calculations is the scattering of photons from the blue emission peak toward the red emission peak. Such P Cygni–type scattering is expected to occur when photons are scattered (and not destroyed) in a geometrically extended region. Figure 11 shows the weighted specific intensity at the Mg II *h* line center (weighted by $2\pi R$ to represent the observed flux from an annulus of radius R) as a function of radius. The stellar disk is relatively dark, as photons have been scattered out of the line of sight, whereas at greater radial distances the intensity increases. This is a result of photons originally scattered out of the line of sight in the wind at negative radial velocities being reemitted at low projected velocities. Note that the weighted intensity is small close to disk center since the area of the annuli are small, while the specific intensity itself may not be small. The observed flux near line center is dominated by the contribution from photons scattered into the line of sight. The maximum radius for $\tau_{\rm Mg\,II\,k} = 1$ in the Mg II *k* line is $\sim 25R_*$, which corresponds to $V = -95$ km s^{-1}. This result confirms that the absorption feature observed at low velocities is interstellar and is insensitive to the location of the wind acceleration since scattering from the wind fills in the intrinsic self-reversal when integrated over the sky. In other stars where the blue emission peak is weak compared to the red peak ($V/R < 1$) (and where this is not due to ISM or line absorption), the wind scattering will also tend to fill in the intrinsic disk projected chromospheric absorption.

Figure 12 shows a model solution for the Mg II *h* line plotted without the observed profile and uncorrected for attenuation by the ISM. Figure 12 shows that the *stellar* (or chromospheric + wind) profile varies smoothly near line center, because the flux comes from a large volume of material. This justifies the use of a smooth intrinsic profile adopted in the ISM study in § 3.

4.3. *Numerical Solution to the Conservation and Momentum Equations*

Very little is known about the nature of mass loss from evolved late-type stars. The velocity distribution derived here for α TrA differs markedly from the results of other investigators studing the ζ Aurigae–type eclipsing binary systems in which the wind is from the more luminous late-type stars. The most recent two-dimensional radiative transfer calculations by Kirsch & Baade (1994) indicate a much larger power-law parameter of $\beta = 3.5$. The problem with such power-law parameterizations is that the physical basis for the velocity law relation is not apparent and it is not clear how the result can be scaled to other stars with different fundamental parameters and levels of activity. In an attempt to place the form of the velocity distribution derived from our line profile fit on a more physical basis, we have computed numerical velocity and density distributions from the combined momentum and conservation equations.

To explore the types of velocity distributions that can result from solutions to the momentum equation, we specify an effective pressure term at a radius R given by

$$P_{\rm eff} = \rho C_{\rm eff}^2 = \rho(C_{\rm thermal}^2 + C_{\rm unknown}^2)\,, \qquad (4)$$

where $\rho C_{\rm thermal}^2$ is the thermal gas pressure and $\rho C_{\rm unknown}^2$ is some as yet unknown nonthermal pressure term, which might be magnetic wave pressure. It is easily demonstrated that thermal pressure cannot be responsible for the observed mass-loss rates (see, for example, Haisch, Linsky, & Basri 1980). The nonthermal pressure term must therefore be responsible for the large density scale heights associated with significant mass-loss rates.

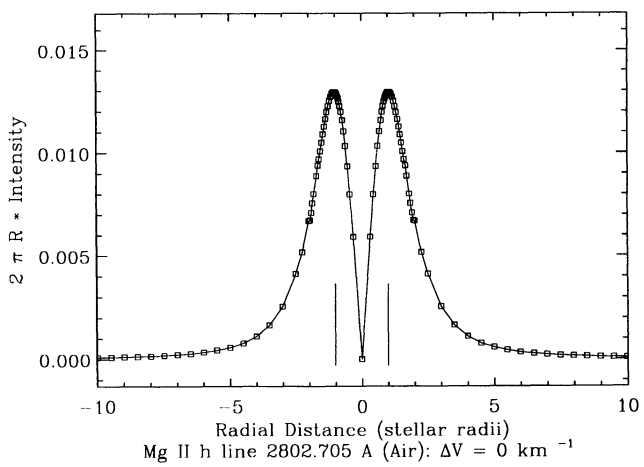

FIG. 11.—The weighted Mg II *h* line center intensity ($2\pi RI$) projected onto the plane of the sky. Note how the observed flux ($\propto 2\pi RI\,dR$) at line center is dominated by photons scattered into the line of sight from a geometrically extended region (see § 4.2.2). The vertical lines indicate the extent of the photospheric disk.

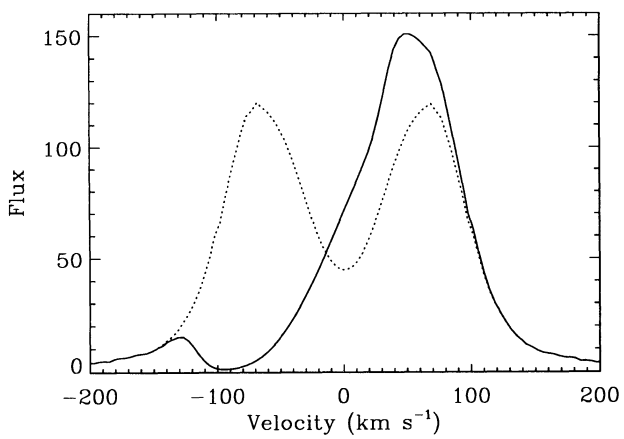

FIG. 12.—The solid line is the computed Mg II *h* line profile, before the ISM absorption and broadening by the *HST* PSF. Note how the flux varies smoothly with wavelength where the ISM absorption components are located. The dashed line is the assumed stellar flux profile which would have been computed in the absence of a stellar wind.

The equations of momentum and continuity can be combined, assuming a time-independent, spherically symmetric flow, to give

$$\frac{dV}{dR}(V^2 - C_{\rm eff}^2) = \frac{V}{R}\left(2C_{\rm eff}^2 - R\frac{dC_{\rm eff}^2}{dR} - \frac{GM_*}{R}\right), \quad (5)$$

where $V = V(R)$ is the flow velocity. We rewrite this momentum equation, using the transformation suggested by Melia (1988) in order to minimize the numerical difficulties experienced when integrating the momentum equation through the critical point. Following Melia (1988) we define

$$\phi(V) \equiv \frac{1}{2}\left(\frac{V}{C_{\rm eff}} + \frac{C_{\rm eff}}{V}\right). \quad (6)$$

Differentiating equation (6) and substituting into equation (5) we obtain the following well-conditioned form suitable for numerical integration,

$$\frac{d\ln\phi}{d\ln R} = \frac{1}{V^2 + C_{\rm eff}^2}\left(N - D\frac{d\ln C_{\rm eff}}{d\ln R}\right), \quad (7)$$

where

$$N = 2C_{\rm eff}^2 - R\frac{dC_{\rm eff}^2}{dR} - \frac{GM_*}{R}, \quad (8)$$

$$D = V^2 - C_{\rm eff}^2. \quad (9)$$

In contrast to integration of the original form of the momentum equation (5), the solutions of equation (7) are all topologically similar in that $\phi(R \approx R_*) \gg 1$, $\phi(R)$ decreases steadily to a minimum near $R = R_{\rm crit}$, and $\phi(R)$ becomes large as $R \to \infty$. The behavior of the critical solution is topologically identical to that of slightly perturbed nearly critical solutions (unlike the case for eq. [5]) and is distinguished by $\phi = \phi_{\rm min} = 1$ at the critical point $R_{\rm crit}$. The solution algorithm used to integrate the critical solution of equation (7) iterates the lower boundary velocity until the minimum value of ϕ equals unity. Our models allowed $C_{\rm eff}(R)$ to ramp up from a constant value near the photosphere to a prescribed maximum value and then decline again. Since $C_{\rm eff}$ is prescribed as a function of radius, the velocity V is given by the appropriate branch of equation (6).

We found that there is only a small range in parameter space that permits solutions resembling a power-law velocity with a small power ($\beta \sim 1$). The criteria for such solutions are (1) $C_{\rm eff} \geq 64$ km s^{-1}, and (2) the rapid increase in $C_{\rm eff}$ occurs close to the surface near $R \sim 1.1R_*$. This latter criterion ensures that the wind velocity is increasing rapidly when $V_{\rm wind} \sim 20$ km s^{-1} *and* that a sufficient absorbing column is produced with reasonable densities above the photosphere. The terminal velocity of the wind depends on how $C_{\rm eff}$ behaves with radius, and, depending on how $C_{\rm eff}$ declines with increasing radial distance, the wind velocities for some solutions gently increase beyond the radius where the Mg II *h* and *k* lines become optically thin.

Although the velocity distributions for different power laws do not match that from the momentum equation, we can derive a crude relationship between $C_{\rm eff}$ and β. Noting that $C_{\rm eff}$ cannot decline too quickly to obtain the desired wind velocities, we assume an *isoturbulent* wind model between the base and the critical radius. The problem then becomes a simple Parker-type wind (see Parker 1960). We further assume that the terminal velocity reaches approximately 2 times the critical velocity, although this last assumption does not strongly affect the following relation. Equating the power law at the critical radius, we find that

$$\beta \sim -\frac{0.6}{\ln\{1 - 10^{-5}[C_{\rm eff}^2(\text{km s}^{-1})R_*(R_\odot)/M_*(M_\odot)]\}}. \quad (10)$$

Clearly, as the velocity of the turbulent elements ($C_{\rm eff} \propto V_{\rm turb}$) approaches the surface escape speed, $\beta \to 0$ as expected. With $C_{\rm eff} = 64$ km s^{-1}, we find that $\beta \simeq 1.1$. The small power-law parameter derived from the Mg II resonance line fits is due in part to the requirement that there not be excessive opacity at low projected velocities. This criterion can also be satisfied by partial (or total) ionization of the wind and a larger value of β (corresponding to smaller $C_{\rm eff}$). This may indeed occur, and when the mass flow is underway one might anticipate a sharp change in projected disk line profile. As we have seen, however, the observed flux at these wavelengths is dominated by photons scattered into the line of sight, and the Mg II resonance lines can provide little further information. It is clear that we can admit a larger set of solutions if $A_{\rm Mg\,II} \neq A_{\rm Mg}$. Constraints on the values of $C_{\rm eff}$ are given in § 5.1.

5. DISCUSSION

The schematic calculations in the present paper indicate a much smaller mass-loss rate than the previously suggested value of $\dot{M} \approx 4$–5×10^{-9} $M_\odot$ yr^{-1} based on constant damping length Alfvén wave wind models (e.g., Hartmann et al. 1981); however, it is closer to more recent values found by different investigators. Note that Jasiński (1987) has modeled Mg II *k* line profiles for five hybrid stars using semiempirical expanding atmospheres. He derived a mass-loss rate for α TrA of 6.12×10^{-9} $M_\odot$ yr^{-1} based on the incorrect assumption that the low-velocity absorption feature observed with the *IUE* is caused by wind rather than by ISM absorption (see our Fig. 3).

The VLA radio flux nondetection for a similar hybrid bright giant, ι Aur (K3 II), gives an upper limit for the mass-loss rate of $\leq 1.7 \times 10^{-9}$ $M_\odot$ yr^{-1} (Drake & Linsky 1986). This observation (Drake & Linsky 1984) led Mendoza (1984) to examine constant damping length Alfvén wave–driven winds for mass-loss rates in the lower range of 10^{-10}–10^{-9} $M_\odot$ yr^{-1}. Mendoza found that to match *IUE* diagnostics, either the wind and high-temperature plasma arose from separate regions in the atmosphere, or the wind acquires more momentum above the line-forming region that is suggested by the constant damping length approach.

Hartmann et al. (1985) and Brosius & Mullan (1986) have both published atmospheric models of α TrA based on the observed emission measures deduced from *IUE* data. While the Hartmann et al. (1985) paper concentrated on hydrostatic models with thermal and turbulent pressure support, the work of Brosius & Mullan (1986) included the wind velocity terms in the momentum equation. Both of these models satisfy electron density constraints from *IUE* data, and the Brosius & Mullan (1986) model predicts transition region line shifts which are small enough to be consistent with the velocity information from the *IUE* data. Figure 9 of Brosius & Mullan (1986) shows that their wind model is consistent with the Hartmann et al. (1985) model. This is expected since at the base of the wind the atmosphere is essentially static, and both approaches should be consistent. Brosius & Mullan (1986) presented a wind model

for α TrA which satisfied a critical point analysis and has the following parameters: $\dot{M} = 8 \times 10^{-10}\ M_\odot\ \mathrm{yr}^{-1}$, $V_\infty = 100$ km s^{-1}. This would be in good agreement with the parameters that we obtain if we allow the wind power-law β to be similar to that found for the ζ Aurigae system. This is plausible since in the Brosius & Mullan (1986) model the transition region flux is formed in the wind, and the Mg II would not be the dominant ionization stage as we have assumed in our analysis. Also, as we have noted previously, the ionization of Mg II would require a larger value of β. The velocity shifts predicted for the transition region emission lines in the Brosius & Mullan (1986) wind model are uncertain but were consistent with the available high-resolution *IUE* data (see, however, the discussion of the C IV in their paper). The velocity information obtained from the analysis of profiles of the emission lines observed in the G200M spectrum confirms the result of previous *IUE* analyses, that there is a strong increase in the atmospheric turbulence with the temperature of line formation. An increase in line width with increasing temperature is predicted by both Alfvén wave and Brosius & Mullan (1986) wind models. The S I lines indicate that $V_{\rm turb} \simeq 14$ km s^{-1} at $\log_{10}(T_e) \simeq 3.8$, whereas the Si III] indicates $V_{\rm turb} \simeq 58$ km s^{-1} at $\log_{10}(T_e) \simeq 4.7$, and the C III] line indicates $V_{\rm turb} \simeq 45$ km s^{-1} at $\log_{10}(T_e) \simeq 4.85$. None of these lines, however, show evidence for systematic velocity shifts in excess of 7 km s^{-1} or gross asymmetries. Indeed, the intersystem lines indicate a possible downflow of 3–7 km s^{-1}. If the small optical depth lines were formed in the stellar wind at a significant fraction of a stellar radius above the surface, then we would expect to observe significant profile asymmetries owing to the geometric occultations of the redshifted emission. If the lines were formed even farther out, they should show flattened profiles, but this characteristic has not been seen in any of the features. The constraint on the electron density from the absence of the quadrupole lines indicates that *if* the transition region intersystem lines form in the wind outflow, they arise at the base of the wind where the densities are high, the wind velocity is very low, and the plasma is highly turbulent. The redshifted intersystem lines would then arise from the averaged difference in emissivities of inflowing and outflowing plasma within the wind. The empirical transition region/wind model of Brosius & Mullan (1986) predicts an upper limit of a 6 km s^{-1} blueshift for the velocity shift of the Si III] line. In § 2.3 we deferred the analysis of the C IV profiles to a future study, but we note that if these lines were formed in the wind they could show a more significant velocity shift towards the blue. We add here that the flux-weighted velocity centroids of the C IV profiles are $\Delta V_{1548} \sim -6$ km s^{-1} and $\Delta V_{1550} \sim +7$ km s^{-1}, and there is no direct evidence for systematic outflow velocities >7 km s^{-1}. It is quite possible that the C IV lines are optically thick and scattered in the wind, but another agent is responsible for the observed profile asymmetries and opposite sense of the velocity centroids.

The model of Brosius & Mullan (1986), which assumes that the transition region is part of the stellar wind, was proposed before the discovery that α TrA is an X-ray source. For a given mass-loss rate an increase in the transition region pressure would lead to a smaller predicted line shift, so that the models of Hartmann et al. (1985) and Brosius & Mullan (1986) could still be consistent with the picture outlined in the work above. If this were the case, the wind would not be represented by a simple homogeneous one-dimensional model. However, detailed line profiles need to be computed rather than simple flux-weighted velocity shifts.

More recently, Harper (1992a) has constructed hydrostatic equilibrium models for the chromospheres and transition regions of these stars and compared the observed Mg II lines with partial redistribution (PRD) radiative transfer calculations. These hybrid-chromosphere models for bright giants were computed to fit the emission-line fluxes of C II, Si II, Al II, and the line profiles and fluxes of the Mg II *h* and *k* lines. One of the main conclusions from his work is that where good profile fits could be made at the base of the emission cores, the line fluxes are too large, whereas profiles that are poor fits to the data are in good agreement with the observed integrated line fluxes. The limitations of such static models are now apparent; the flux in the red emission peak appears to contain a significant contribution from scattering by ions in the stellar wind in a geometrically extended region. Therefore, matching this peak flux with a static model must lead to an overestimate of the temperature gradient, which implies that an adjustment in the density stratification is needed to match the fluxes from the other emission lines.

Our simulations suggest that the wind absorption feature is formed at a radial distance where there is a small velocity gradient and thus a large line opacity. We also find that the microturbulent velocity for the best-fit model is much smaller than the terminal velocity. This indicates that more detailed modeling of this wind will require that radiative transfer in the Mg II *h* and *k* lines be calculated with partial redistribution (in the comoving frame). Such calculations for α Boo (K2 III) have been made by Drake (1985), who estimated a mass-loss rate of $2 \times 10^{-10}\ M_\odot\ \mathrm{yr}^{-1}$, a value similar to the rate we have determined for α TrA. Mass-loss rates of this magnitude are too small to change the evolution of stars like α TrA, either on their first crossing of the Hertzsprung gap (see Simon, Linsky, & Stencel 1982), which is less than 10^6 yr for a star of $5\ M_\odot$ (Iben 1966), or during the helium burning phase, which occupies 10^7 yr (Iben 1967).

The wind velocity distribution we adopted in modeling the Mg II resonance lines is a monotonically increasing power law. It is possible, however, that the wind reaches a maximum velocity and then decreases under the influence of gravitational attraction. Carpenter (1984) found tentative evidence for such a flow pattern from *IUE* observations of Fe II emission-line asymmetries in α Ori, but more recent GHRS observations do not exhibit the same structure (Carpenter et al. 1994). Although constant-β velocity laws have been used to model the winds of the cool star components of ζ Aur systems, the wind densities and velocities in these systems are likely to be affected to some extent by the orbital and gravitational interaction of the companion B star (both stellar components have similar masses).

5.1. *Further Velocity Constraints*

If the observed turbulent motions, $V_{\rm turb}$, are interpreted as isotropic with spatial scales smaller than the pressure scale height, then we can identify $P_{\rm turb} = 0.5\rho V_{\rm turb}^2$, where $V_{\rm turb} = \sqrt{2C_{\rm eff}}$ in § 4.3. For the small values of $\beta \leq 1$ the values of the implied $V_{\rm turb}$ greatly exceeds those seen in the Si III] and C III] lines. e.g., for $\beta \simeq 1.1$ this would require $V_{\rm turb} \sim 89$ km s^{-1}; however, $V_{\rm turb} \simeq 80$ km s^{-1} for the less opaque C IV line.

If the wind is partially ionized, larger values of β are acceptable and are more compatible with the line widths seen in the transition region lines. It seems probable that these line widths are associated with the energy deposition at the base of the wind, but we cannot yet determine whether or not they are part of the wind flow. It is not coincidental that the Alfvén wave

model of Hartmann et al. (1981) shows similar velocity behavior to that of our momentum equation analysis in § 4.3. In their model, the large scale height at the base of the wind is associated with the Alfvén-wave pressure balancing gravitational acceleration, which is being manifested in velocities corresponding to the amplitude of the Alfvén waves. The same conclusion also holds for the line widths in the model of Brosius & Mullan (1986).

In the absence of significant radiative acceleration, in *any* one-dimensional homogeneous time-independent wind model, the values of $C_{\rm eff}$ (see § 4.3) associated with the large scale-heights (required to match observations) must greatly exceed the chromospheric thermal velocities. $C_{\rm eff}$ will be manifested as large velocity motions at the base of the wind. We expect that large turbulent motions are a necessary consequence of the mechanisms responsible for the observed mass-loss rates.

We have computed schematic optically thin line profiles for the above wind models and find that models with $\beta \leq 0.8$ can, for certain specific temperature stratifications, show blue-shifted flux centroids inconsistent with the observed Si III] profile. GHRS echelle spectra will be required, however, to distinguish between the small line shifts predicted in winds with smaller accelerations (larger β) and plasma that is confined near the surface. These observations should provide information to help resolve the question of whether the wind acquires temperatures high enough to produce the observed Si III] and C III] lines ($T_e \geq 4 \times 10^4$). Radio observations at 3.6 cm and 6 cm would also be useful to constrain the ionization balance of the wind.

5.2. *Other Diagnostics*

5.2.1. Ca II K *Line*

To gain further insight into the regions of low velocity we need to examine scattering in lines with smaller ISM attenuation and smaller opacities, such as the Ca II K line (3933.663 Å). The α TrA line profiles shown by Reimers (1982); Pasquini, Pallavicini, & Pakull (1988); and Zarro & Rodgers (1983) show that at least part of the blue emission peak is still present. We have, therefore, repeated the above calculations for the Ca II K line to see whether this line profile can limit the range of possible solutions. Adopting an abundance of $A_{\rm Ca} = 1.7 \times 10^{-6}$ (Kovács 1983), we find that if Ca II is the dominant ionization state throughout the wind, then the power-law relation cannot reproduce the observed profiles unless $\beta < 0.1$, which implies an almost impulsive acceleration. The expected ISM attenuation of the Ca II K line is not significant. Other emission lines observed in *IUE* echelle spectra which form in the region where the Ca II K line photons escape the atmosphere do not show such large velocity shifts. We believe that the most probable explanation is that calcium is predominantly Ca III.

To investigate this possibility we would need to examine line profiles such as the C II 1335 Å multiplet and the O I 1304 Å triplet. Neutral oxygen and singly ionized carbon should be the dominant ionization stages when magnesium is singly ionized. If $\beta = 0.8$, then we find that the relative abundance of Ca II must be $A_{\rm Ca\,II} < 0.1 A_{\rm Ca}$ in the acceleration region so that the Ca II K line blue emission peak photons are not appreciably scattered. A comparison of the ionization mechanism for Ca II → Ca III and Mg II → Mg III shows that in addition to the lower ionization potential of Ca III, the Ca II $3\,^2D$ metastable level provides additional paths for Ca III to form at lower temperatures than for Mg III. In particular, H Lyα (Linsky & Avrett 1970) and the C II recombination continuum (which also ionizes S I) lie shortward of the Ca II $3\,^2D$ ionization edge at 1219 Å and may provide additional ionization paths.

5.2.2. *Hydrogen Diagnostics*

The Hα profile of Zarro & Rodgers (1983) shows little asymmetry, suggesting that the wind is optically thin to Hα. The opacity of Hα is, however, very sensitive to the temperature through the collisional excitation of the $n = 2$ level which limits the diagnostic potential of this line. The total column of hydrogen from the *IUE* analysis of the Lyα profile ($N_{\rm H\,I} \simeq 3 \times 10^{19}$ cm^{-2}) reported in Kashyap et al. (1994) is consistent with the ISM column values derived from the Mg II *h* and *k* line profiles. The value inferred from an X-ray analysis (Kashyap et al. 1994) also is consistent with this value, which suggests that the X-ray photons are not formed in embedded regions deep within the mostly neutral chromosphere. Ayres & Kashyap (1994) present tentative evidence for a high-speed wind (400 km s^{-1}) from the marked asymmetry of the high-resolution H Lyα profile obtained with *IUE*. Their analysis assumed a pure absorption model for the wind but neglected scattering of photons into the line of sight, which is known to be imporatant for the analysis of the Mg II *h* and *k* line profiles. If the Lyα $\tau = 1$ scattering surface is unresolved with the *IUE* aperture, then this may affect the conclusions of Ayres & Kashyap (1994). The angular size of the maximum Mg II *k* $\tau = 1$ surface is approximately 0".31, which is well within the GHRS LSA but larger than the SSA. Figure 11, however, suggests that most of the stellar flux will be collected in SSA observations. If hydrogen were mainly neutral, then the Lyα scattering region will not be resolved with either the LSA or SSA. A differential comparison of Lyα SSA and LSA observations may allow us to place constraints on the ionization balance of hydrogen. We note that depending on the nature of the energy flux in the wind, it is possible that the wind may continue to accelerate beyond the Mg II $\tau = 1$ scattering surface to velocities > 100 km s^{-1}.

6. CONCLUSIONS

The GHRS observations of the Mg II resonance lines show two ISM features that are not resolved with high-resolution *IUE* observations. Wind models of the high-velocity wind absorption features suggest a lower limit to the mass-loss rate of $1.6 \times 10^{-10}\ M_\odot$ yr^{-1} which is significantly smaller than that found from early constant damping length Alfvén wave models for α TrA but closer to more recent values found by different investigators. Our models also show that the flux observed close to the line centers of these resonance lines comes from scattering in an extended region and confirms that the low-velocity narrow absorption features are interstellar rather than a chromospheric self-reversal. The main uncertainties in the wind model presented here are the ionization of Mg and the rate of acceleration of the wind above the chromosphere. Numerical models of the momentum and conservation equations suggest that in order to have sufficient column density to produce the observed Mg II wind scattering, the density scale height at the base of the wind must greatly exceed chromospheric thermal scale heights. The *magnitude* of turbulent motions expected to be associated with the wind density and velocity structure is similar to those observed in the Si III] and C III] transition region lines, although the observed values are smaller than expected if Mg II is the dominant ionization stage in the wind.

The 1993 February (pre-COSTAR) LSA observation of the Mg II resonance line profiles shows a reflection asymmetry about the line centers in the stellar rest frame. The wind models for this observation require either the use of multiple components to match the far wing profiles *or* that the intrinsic line profiles are not centered in the stellar rest frame. The more recent (post-COSTAR) SSA observation shows reflection symmetry and a single-component wind model can satisfactorily match the observed profile.

The next step toward more physical models for the expanding atmosphere of late-type stars is to construct complete atmospheric models that match several different diagnostics (e.g., Harper 1992a) and include the dynamical effects of the wind (e.g., Jasiński 1987). The velocity and density structure should be determined from the momentum equation, given pressure gradients and other proposed wind acceleration mechanisms. For the resonance line diagnostics a more realistic treatment of photon scattering is also required (e.g., Drake 1985). A semiempirical determination of the velocity structure should help us understand the presently unknown wind-accelerating mechanisms in evolved late-type stars. Construction of such models is now in progress. Improved stellar parameters are also urgently required, and when the *HIPPARCOS* parallaxes become available we should be able to determine the distance more reliably. This will allow us to derive the stellar radius from the well-constrained angular diameter, which is of significant importance to the accuracy of radiative transfer calculation in spherical atmospheres. As shown in § 4.2.1 the uncertainty in the stellar radius remains a significant systematic error. In the final analysis, the high quality of the *HST* data has raised more questions than we have as yet answered.

We would like to thank an anonymous referee for helpful suggestions which have improved the clarity of this manuscript. This work is supported by NASA grant S-56460-D to the National Institute of Standards and Technology, STScI grant GO-5323.01-93A and NASA grant NAGW-2904. This research has made use of the SIMBAD database, operated at CDS, Strasbourg, France.

REFERENCES

Anders, E., & Grevesse, N. 1989, Geochim. Cosmochim. Acta, 53, 197
Ayres, T. R. 1985, ApJ, 291, L7
Ayres, T. R., & Kashyap, V. 1994, in Cool Stars, Stellar Systems, and the Sun, 8th Cambridge Workshop, ed. J.-P. Caillault (ASP Conf. Ser., 64), 681
Ayres, T. R., Linsky, J. L., Vaiana, G. S., Golub, L., & Rosner, R. 1981, ApJ, 250, 293
Ayres, T. R., et al. 1995, ApJS, 96, 223
Baade, R. 1992, in Stellar Chromospheres, Coronae, and Winds, ed. C. S. Jeffery & R. E. M. Griffin (Cambridge: IOA), 49
Berrington, K. A. 1985, J. Phys. B, 18, L3956
Berrington, K. A., Burke, P. G., Dufton, P. L., & Kingston, A. E. 1985, At. Data Nucl. Data Tables, 33, 195
Bertaux, J. L., Lallement, R., Kurt, V. G., & Mironova, E. N. 1985, A&A, 150, 82
Brandt, J. C., et al. 1994, PASP, 106, 890
Brosius, J. W., & Mullan, D. J. 1986, ApJ, 301, 650
Brown, A., Drake, S. A., van Steenberg, M. E., & Linsky, J. L. 1991, ApJ, 373, 614
Brown, A., Reimers, D., & Linsky, J. L. 1986, in New Insights in Astrophysics (ESA SP-263), 169
Burton, R. B., 1991, M.S. thesis, Univ. of Colorado
Butler, S. E., & Dalgarno, A. 1980, A&A, 85, 144
Carpenter, K. G. 1984, ApJ, 285, 181
Carpenter, K. G., Robinson, R. D., Wahlgren, G. M., Ake, T. B., Ebbets, D. C., Linsky, J. L., Brown, A., & Walter, F. M. 1991, ApJ, 377, L45
Carpenter, K. G., Robinson, R. D., Wahlgren, G. M., Linsky, J. L., & Brown, A. 1994, ApJ, 428, 329
Crutcher, R. M. 1982, ApJ, 253, 82
Doyle, J. G. 1987, At. Data Nucl. Data Tables, 37, 441
Drake, S. A. 1985, in Progress in Stellar Spectral Line Formation Theory, ed. J. E. Beckman & L. Crivellari (Dordrecht: Reidel), 351
Drake, S. A., Brown, A., & Linsky, J. L. 1984, ApJ, 284, 774
Drake, S. A., & Linsky, J. L. 1984, private communication
———. 1986, AJ, 91, 602
Dufton, P. L., & Kingston, A. E. 1989, MNRAS, 241, 209
Duncan, D. K. 1992, Goddard High-Resolution Spectrograph Instrument Handbook, Version 3.0 (Baltimore: STScI)
Ebbets, D. C. 1992, in Final Report of the SV Program from the GHRS for the *HST* (Boulder: Ball Aerospace Systems Group)
Fleming, J., Hibbert, A., & Stafford, R. P. 1994, Phys. Scripta., 49, 316
Froese-Fischer, C. 1994, Phys. Scripta, 49, 323
Gilliland, R. L., & Hulbert, S. J. 1993, GHRS Instrument Sci. Rep. 55
Haisch, B. M., Linsky, J. L., & Basri, G. S. 1980, ApJ, 235, 519
Haisch, B. M., Schmitt, J. H. M. M., & Rosso, C. 1991, ApJ, 383, L15
———. 1992, ApJ, 388, L61
Harper, G. M. 1992a, MNRAS, 256, 37
———. 1992b, in Stellar Chromospheres, Coronae, and Winds, ed. C. S. Jeffery & R. E. M. Griffin (Cambridge: IOA), 73
Harper, G. M. 1994, MNRAS, 268, 894
Hartmann, L., Dupree, A. K., & Raymond, J. C. 1980, ApJ, 236, L143
———. 1981, ApJ, 246, 193
Hartmann, L., Jordan, C., Brown, A., & Dupree, A. K. 1985, ApJ, 296, 576
Hartmann, L., & McGregor, K. B. 1980, ApJ, 242, 260
Hubeny, I. 1988, Comput. Phys. Commun., 52, 103
Iben, I., Jr. 1966, ApJ, 143, 483
———. 1967, ARA&A, 5, 425
Idrees, M., & Das, B. P. 1989, J. Phys. B, 22, 3609
Jasiński, M. 1987, Acta Astron., 37, 1
Jordan, C. 1967, Sol. Phys., 2, 441
Judge, P. G. 1988, MNRAS, 231, 419
———. 1990, ApJ, 348, 279
———. 1994, ApJ, 430, 351
Kashyap, V. L. 1993, Ph.D. thesis, Univ. of Chicago
Kashyap, V. L., Rosner, R., Harnden, F. R., Jr., Maggio, A., Micela, G., & Sciortino, S. 1994, ApJ, 431, 402
Kaufman, V. 1982, Phys. Scripta, 26, 439
Kirsch, T., & Baade, R. 1994, A&A, 291, 535
Kovács, N. 1983, A&A, 120, 21
Krogulec, M. 1989, Acta Astron., 39, 51
Kwong, H. S., Johnson, B. C., Smith, P. L., & Parkinson, W. H. 1983, Phys. Rev. A, 27, 3040
Kwong, V. H. S., Fang, Z., Gibbons, T. T., Parkinson, W. H., & Smith, P. L. 1993, ApJ, 411, 431
Lallement, R., & Bertin, P. 1992, A&A, 266, 479
Lallement, R., Vidal-Madjar, A., & Ferlet, R. 1986, A&A, 168, 225
Lenz, D. D., & Ayres, T. R. 1992, PASP, 104, 1104
Linsky, J. L. 1982, in Advances in Ultraviolet Astronomy: Four Years of *IUE* Research (NASA CP-2238), 17
Linsky, J. L., & Avrett, E. H. 1970, PASP, 82, 169
Linsky, J. L., Brown, A., Gayley, K., Diplas, A., Savage, B. D., Ayres, T. R., Landsman, W., Shore, S. N., & Heap, S. R. 1993, ApJ, 402, 694
Linsky, J. L., & Haisch, B. M. 1979, ApJ, 229, L27
Linsky, J. L., Wood, B. E., & Andrulis, C. 1994, in Cool Stars, Stellar Systems, and the Sun, 8th Cambridge Workshop, ed. J.-P. Caillault (ASP Conf. Ser., 64), 681
Linsky, J. L., Wood, B. E., Judge, P. G., Brown, A., Andrulis, C., & Ayres, T. R. 1995, ApJ, 442, 381
Mayor, M., & Maurice, E. 1985, in IAU Colloq. No. 88, Stellar Radial Velocities, ed. A. G. D. Philip & D. W. Lathum (Schenectady, NY: Davis), 300
Melia, F. 1988, J. Comput. Phys., 74, 488
Mendoza, B. E. 1984, Ph.D. thesis, Oxford Univ.
Moore, C. E., Brown, C. M., Sandlin, G. D., Tilford, S. G., & Tousey, R. 1977, ApJS, 33, 393
Morton, D. C. 1991, ApJS, 77, 119
Ng, K.-C. 1974, J. Chem. Phys., 61(7), 2680
Nussbaumer, H. 1986, A&A, 155, 205
Nussbaumer, H., & Storey, P. J. 1978, A&A, 64, 139
Ojha, P. C., Keenan, F. P., & Hibbert, A. 1988, J. Phys. B, 21, L395
Parker, E. N. 1960, ApJ, 132, 175
Pasquini, L., Pallavicini, R., & Pakull, M. 1988, A&A, 191, 253
Rao, L., Baliunas, S. L., Robinson, C. R., Frazer, W. L., & Donahue, R. A. 1993, in Luminous High-Latitude Stars Workshop, ed. D. D. Sasselov (ASP Conf. Ser., 45), 300
Reimers, D. 1982, A&A, 107, 292
Simon, T., Linsky, J. L., & Stencel, R. E. 1982, ApJ, 357, 225
Stencel, R. E., & Mullan, D. J. 1980a, ApJ, 238, 221
———. 1980b, ApJ, 240, 718
Zarro, D. M., & Rogers, A. W. 1983, ApJS, 53, 815